A compressible two-phase flow framework for Large Eddy Simulations of liquid-propellant rocket engines

Clement Le Touze, Luc-Henry Dorey, Nicolas Rutard, Angelo Murrone

To cite this version:

Clement Le Touze, Luc-Henry Dorey, Nicolas Rutard, Angelo Murrone. A compressible two-phase flow framework for Large Eddy Simulations of liquid-propellant rocket engines. Applied Mathematical Modelling, 2020, 84, pp.265-286. 10.1016/j.apm.2020.03.028 . hal-02750951

HAL Id: hal-02750951
https://hal.science/hal-02750951v1

A compressible two-phase flow framework for Large Eddy Simulations of liquid-propellant rocket engines

C. Le Touze[a,*], L.-H. Dorey[a], N. Rutard[a], A. Murrone[a]

[a] *DMPE, ONERA, Université Paris-Saclay, F-91123 Palaiseau - France*

Abstract

Atomization of liquid jets is a key feature of many propulsion systems, such as jet engines, internal combustion engines or liquid-propellant rocket engines (LRE). As it controls the characteristics of the spray, atomization has a great influence on the complex interaction between phenomena such as evaporation, turbulence, acoustics and combustion. In this context, Computational Fluid Dynamics is a promising way to bring better understanding of dynamic phenomena involving atomization, such as e.g. high-frequency combustion instabilities in LRE. However the unsteady simulation of primary atomization in reactive compressible two-phase flows is very challenging, due to the variety of the spatial and temporal scales, as well as to the high density, velocity and temperature gradients which require robust and efficient numerical methods. To address this issue, a numerical strategy is proposed in this paper, which is able to describe the dynamics of the whole chain of mechanisms from the liquid injection to its atomization and combustion. Primary atomization is modeled by a coupling between a homogeneous diffuse interface model and a kinetic-based Eulerian model for the spray. This strategy is successfully applied to the unsteady simulation of an operating point of the ONERA's MASCOTTE test bench, representative of one coaxial injector of LRE operating under subcritical conditions. The dynamics of the liquid core is retrieved and the flame shape as well as Sauter mean diameters are in good agreement with experimental results. These results demonstrate the ability of the strategy to deal with the harsh conditions of cryogenic combustion, and provide a promising framework for future studies of combustion instabilities in LRE.

Keywords:
Compressible multiphase flows, Atomization and sprays, Cryogenic combustion, Large Eddy Simulation, Unstructured finite volume code, Liquid-propellant rocket engines

---

1. Introduction

High-pressure reactive two-phase flows (TPF) are present in a large variety of propulsion systems and Computational Fluid Dynamics (CFD) is more and more used to better understand and manage them, in jet

---

[*] Corresponding author
Email address: `cletouze@onera.fr` (C. Le Touze)

engines [1], internal combustion engines [2, 3], or liquid-propellant rocket engines (LRE) [4, 5]. Realistic and accurate numerical simulation of full-scale devices remains a challenge for CFD, as large ranges of spatial and temporal scales are involved, along with numerous physical phenomena and strong gradients of physical properties (e.g. density, temperature or velocity). Specific frameworks, such as the one proposed in this paper, have to be designed in order to predict the dynamic behavior of all phenomena at play in such flows.

In the context of LRE, CFD is a promising way to better understand High Frequency (HF) combustion instabilities, which still remain poorly understood, and to formulate reduced-order models for industrial design. HF combustion instabilities are high-amplitude pressure oscillations that can lead to the destruction of the rocket engine and the failure of the mission. They involve strongly coupled unsteady phenomena that are challenging to model accurately, especially in real engines [6].

Recent Large Eddy Simulations (LES) have brought a new level of understanding in the case of oxidizer injected either in the gaseous state [7, 8] or in transcritical conditions [4, 9]. But CFD has not reached the same level of maturity in the case of oxidizer injected in subcritical conditions (i.e. in liquid phase), while such conditions are involved in transient and low thrust operating phases in which HF instabilities may be triggered. Even though a few numerical studies [5, 10] addressed this issue in the past, LES methods do not yet seem to be used to investigate HF instabilities in subcritical conditions, mainly because specific strategy and modeling are required. This paper is then focused on the unsteady simulation of high-pressure reactive TPF encountered in LRE operating at subcritical conditions. In this case, the liquid flow is subject to large changes in its topology, as mapped in Fig. 1: downstream the coaxial injector, liquid oxygen (LOX) is sheared by the high-velocity co-flowing gas flow, e.g. gaseous hydrogen (GH_2) as in Fig. 1, or gaseous methane (GCH_4). This entails a TPF of complex topology [11] in which three areas can be highlighted:

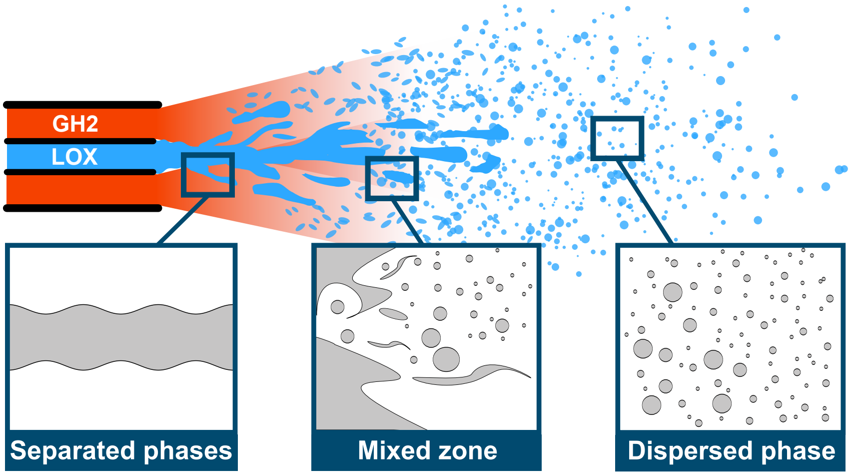

Figure 1: Schematic representation of the two-phase flow at the exit of a coaxial cryogenic injector in subcritical conditions. (Color online.)

- a “separated phases” TPF near the injector exit where the interface remains rather stable,
- a “mixed” TPF where primary atomization takes place: interface is wrinkled and ligaments are detached from the main liquid core,
- a “dispersed phase” TPF once secondary break-up has given rise to a spray of small LOX droplets, dispersed by the turbulent gas flow and vaporized to feed the combustion with the fuel.

Understanding the interactions between all physical phenomena (propellant injection, atomization, evaporation, combustion, turbulence and acoustics) is of major importance to predict and mitigate HF instabilities. In particular, the dynamics of the dense liquid core and its subsequent atomization are known to be strongly coupled to acoustics [12], and also to the flame behavior [13]. In order to reach a better understanding and control of these complex phenomena, it is therefore necessary to develop, together with experimental devices, CFD tools able to accurately and efficiently describe all the TPF topologies and dynamics in a reactive context.

To achieve this goal, DNS tools combined with interface tracking or capturing methods, such as Level Set and Volume Of Fluid methods, have provided very promising results [14–20]. Nevertheless, despite the continuous increase in computational resources, it seems that such DNS approaches are still too expensive to tackle industrial configurations, especially when considering atomization of the jet combined with the combustion of the spray and acoustics. Leaving DNS aside, the seminal work of Vallet et al. [21] has initiated the effort to include primary atomization modeling within the RANS formalism together with diffuse interface methods. It was pursued afterwards by many studies, mostly applied to internal combustion engines but also sometimes to cryogenic rocket engines [5, 22, 23]. All these works include a transport equation for the liquid-gas surface density area. Dedicated source terms describe both interface creation and destruction, and are closed by means of subgrid models derived from theoretical, experimental or DNS results [19]. The surface density equation strategy has also been employed in the LES context coupled with interface tracking methods [24].

As a sequel to the above-mentioned works, the idea arose of coupling the surface density equation strategy with a dedicated Lagrangian description of the dispersed phase, as employed for instance by Lebas et al. [2]. The objective was then to reach a better overall accuracy by allowing the spray to be described with its own variables and equations, rather than describing it only through the surface density equation and the mean properties of the whole subgrid liquid-gas mixture. However, operating the transition towards the Lagrangian formalism to account for the spray formation is not without difficulties [25]. On the other hand, a fully Eulerian formalism could well offer a more natural and robust coupling framework when describing primary atomization.

The objective of the present work is thus to introduce a very new fully Eulerian coupling strategy for the simulation of unsteady compressible multiphase reacting flows, involving the primary atomization of liquid jets. The numerical framework is described in section 2 in terms of governing equations. It requires the development of an original modeling accounting for primary atomization, which is introduced in section 3. Finally, the simulation of a cryogenic flame in subcritical conditions is presented in section 4. This last section illustrates how the methodology works, gives some insights of the TPF features and dynamics in such applications, and provides some comparisons with experimental measurements. Through this section and associated discussions, the capacity of the novel methodology proposed in this paper to simulate realistic cryogenic flows with representative results is demonstrated.

2. Eulerian-Eulerian coupling strategy

2.1. General description

The modeling strategy implemented in ONERA's CEDRE simulation platform [26], is illustrated in Fig. 2 when applied to the case of LOX-GH_2 combustion. A *Separated Phases* Solver (SPS), called CHARME, solves the compressible Navier-Stokes equations in a LES context for a flow that may locally comprise a turbulent reactive multi-species gas phase, a liquid phase made up with only the LOX species, or a two-phase homogeneous mixture with a diffuse interface approach. When equipped with a sufficiently refined mesh for LES, the SPS is able to describe the dynamics of the dense liquid core downstream of the injector exit, the triggering of interfacial instabilities at its surface, as well as the peeling of some ligaments and large droplets. However, as the atomization process produces smaller and smaller droplets, these become far too small to be captured by a reasonable mesh. This is why the choice is then made to operate a transfer towards a *Dispersed Phase* Solver (DPS), called SPIREE, which is a kinetic-based Eulerian solver for the spray. Indeed, rather than pursuing the description of the spray at the subgrid scale level with the SPS, the DPS provides a more accurate framework by solving appropriate conservation equations on dedicated variables for the spray. It also includes a description of the droplet size polydispersion thanks to the sectional method with affine reconstruction [27, 28]. A reverse transfer towards the SPS accounts for evaporation, thereby feeding the gas phase with GO_2 and enabling combustion. Both solvers are thus coupled by exchanging with one another source terms that depend on the local features of the flow. This means that the exact location of the coupling phenomena depicted in Fig. 2 is not prescribed, but naturally evolves throughout the computation.

2.2. Governing equations for the separated phases

The compressible Navier-Stokes equations solved by the SPS for a multi-species homogeneous mixture can be written in vector form as

$$\partial_t \boldsymbol{Q} \,+\, \nabla.\left(\boldsymbol{F} - \boldsymbol{\varphi}\right) \,=\, \boldsymbol{S}\,, \tag{1}$$

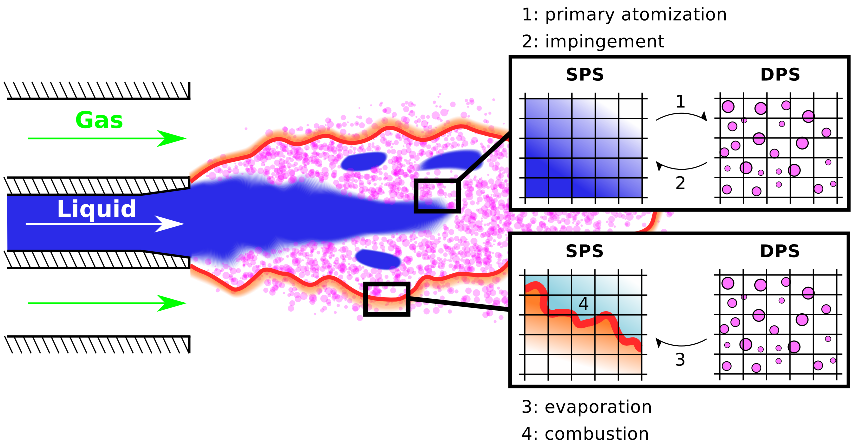

Figure 2: Schematic view of the coupling strategy between the SPS and the DPS. (Color online.)

where $\boldsymbol{Q} = (\rho Y_1 \;\; ... \;\; \rho Y_{N_g} \;\; \rho Y_l \;\; \rho \boldsymbol{u} \;\; \rho e_t)^t$ is the vector of the conservative variables, comprising the partial densities, momentum and total energy of the mixture, while $\rho = \sum_i (\rho Y_i)$ is the density of the whole mixture. From $\boldsymbol{Q}$, one can derive a set of primitive variables $\boldsymbol{U} = (Y_1 \;\; ... \;\; Y_{N_g} \;\; Y_l \;\; \boldsymbol{u} \;\; P \;\; T)^t$, i.e. the mass fractions of the N_g gas species plus that of the liquid, as well as the mixture mean velocity, pressure and temperature.

The vector of the convective fluxes $\boldsymbol{F}$ is that of the standard compressible Euler equations, which can be written in the form

$$\boldsymbol{F} \;=\; \boldsymbol{Q} \otimes \boldsymbol{u} \,+\, P \, (0 \;\; ... \;\; 0 \;\; 0 \;\; \boldsymbol{I}_3 \;\; \boldsymbol{u})^t \, , \tag{2}$$

with $\boldsymbol{I}_3$ the 3D unit tensor. The vector of the diffusive fluxes $\boldsymbol{\varphi}$ may include laminar and turbulent diffusion fluxes. For instance, Fourier's and Fick's laws are classically used to describe the laminar diffusion of heat and species respectively, while the divergence of the viscous stress tensor accounts for the laminar diffusion of momentum. In a LES context, additional diffusion terms can be added to account for the dissipation of the turbulent kinetic energy at the subgrid scale level (for instance through the Boussinesq's concept of eddy-viscosity together with the Smagorinsky model), although this point is not so easy a task when it comes to compressible reactive two-phase flows [29]. If significant capillary effects are expected, then a modeling of the surface tension forces can also be included, e.g. by means of the CSF approach [30]. This must be considered on a case-by-case basis, depending on the Weber numbers involved. Furthermore, the vector $\boldsymbol{S}$ includes all source terms relevant to the configuration to simulate. In the context of the paper, this means at least chemical combustion rates and coupling terms with the dispersed phase, as detailed in section 2.4.

The thermodynamic closure of the system is based on the assumption of thermal and mechanical equilibrium between phases [31, 32], together with dedicated equations of state for each phase. The gas phase is then modeled as an ideal gas mixture, leading to

$$\rho_g(P,T) = \frac{P}{RT}\left(\sum_{i=1}^{N_g} Y_i/W_i\right)^{-1} , \tag{3}$$

with ρ_g the density of the gas phase, R the ideal gas constant and W_i the molar mass of a given gaseous species i. The equation of state for the liquid phase is a barotropic (isothermal) linearised equation of state, already used for instance in [33], which reads

$$\rho_l(P) = \rho_0\left[1 + \beta_0(P - P_0)\right] , \tag{4}$$

with ρ_l the density of the liquid phase and β_0 its isothermal compressibility at a given reference state (ρ_0, P_0), or similarly

$$P(\rho_l) = P_0 + c_l^2\left(\rho_l - \rho_0\right) , \tag{5}$$

where $c_l = (\beta_0\rho_0)^{-1/2}$ is the constant sound speed of the liquid phase. This equation of state is accurate in the limit of small variations around the reference state (ρ_0, P_0), and restricted to the pure liquid area of the phase diagram. Next, mass-fraction-weighted average values of density and internal energy can be computed for the two-phase mixture, and used in an iterative process to recover the updated equilibrium pressure and temperature. In addition, the liquid phase volume fraction α_l can be introduced as well. Due to the thermal and mechanical equilibrium assumption, this is not an independent transported variable of system (1), but can be straightforwardly obtained from the liquid mass fraction and the densities of pure phases as follows:

$$\alpha_l = \frac{\rho Y_l}{\rho_l} = \frac{\rho_g Y_l}{\rho_g Y_l + \rho_l(1 - Y_l)} . \tag{6}$$

Note that in the terminology of TPF models, the SPS solves a diffuse interface model very similar to the homogeneous relaxation model (sometimes referred to as the 4-equation model) [31, 34], but without considering any mass transfer between phases at this level. Evaporation is then only considered in the DPS, once the liquid is in the form of droplets. Also note that the homogeneous relaxation model can be formally obtained by a relaxation of the more general 7-equation diffuse interface model, by means of an asymptotic analysis based on the Chapman-Enskog theory [11, 35–37]. Finally, it should be stressed that the use of this 4-equation model for the SPS has both advantages and drawbacks. As this model is nothing else than the multi-species compressible Navier-Stokes equations, it is widely used in classical CFD codes based on the finite volume method, which more easily include the whole complexity required for an application to HF instabilities in LRE than specialized codes solving accurate diffuse interface models. Indeed, the former are more likely to include e.g. turbulent combustion modeling, complex thermodynamics and advanced numerical methods than the latter. Nevertheless, it is clear that the eventual use of these more accurate diffuse interface models, giving locally access e.g. to the temperature and the velocity of each phase, as well as to some geometrical variables describing the interface topology at the subgrid scale level, will provide the necessary matter for an important step forward in the modeling of the primary atomization. However, a significant work is required to bring these models to the level of maturity that would make them fully compatible with real simulations in a reactive context. This means for instance defining proper modeling closures to the system and dedicated numerical schemes, which is a work in progress (see [38–40]).

2.3. Governing equations for the dispersed phase

The Eulerian system of conservation equations for the spray can be formally derived from the kinetic level. Indeed, at the highest level of description, the modeling of dispersed two-phase flows is based on a mesoscopic description provided by the Williams-Boltzmann kinetic equation (WBKE) [41]. This equation gives the evolution of the probability density function f for the number of droplets per unit volume, also called the number density function (NDF). Assuming the particles spherical and fully characterized at a given time t by a set of variables on which the NDF depends, for instance their position x, their size s (radius, diameter, surface...), their velocity $\boldsymbol{v}$ and their temperature θ, then the WBKE expressing the conservation of the NDF $f\left(t, \boldsymbol{x}, \boldsymbol{v}, s, \theta\right)$ in the phase space reads in

$$\partial_t f + \nabla_{\boldsymbol{x}} \cdot (\boldsymbol{v} f) + \nabla_{\boldsymbol{v}} \cdot (\boldsymbol{\mathcal{F}} f) + \partial_s \left(\mathcal{K} f\right) + \partial_\theta \left(\mathcal{R} f\right) = \Gamma \,. \tag{7}$$

The left-hand-side of the WBKE describes the transport of the particles in the phase space ($\boldsymbol{\mathcal{F}}$, $\mathcal{K}$ and $\mathcal{R}$ respectively correspond to the force acting on a particle, the evaporation rate and the heat exchange rate), while Γ on the right-hand-side stands for the fragmentation phenomenon, which is a non-conservative contribution to the NDF evolution. The direct resolution of the WBKE is however out of reach for practical applications because of the highly dimensional phase space. This is why in practice, the Eulerian methods rather solve transport equations for some particular moments of the NDF, thereby proceeding to a reduction of the phase space (see [42] for a comprehensive review on Eulerian moment methods).

An important part of this reduction process consists in discretizing the particle size distribution. To do so, several approaches have been developed in the framework of Eulerian moment methods. Of these, the sectional method [43–45] has been selected here for its natural ability to account for phenomena that generate polydispersion, such as secondary break-up and evaporation. In the sectional approach, the size space $[0, +\infty[$ is discretized into N_s contiguous intervals $[s_{k-1}, s_k[$ called *sections*, and the mathematical shape of the particle size distribution within each section k has to be postulated. Among the several options available in the literature for that purpose, the affine-TSM (Two Size Moment) method has been retained in this paper because it seems to offer the best compromise between accuracy and computational cost, as well as the advantage of satisfying some realizability and positivity constraints [27, 28]. In the affine-TSM method, the number size distribution $\phi^k_{n,S}(S)$ in each section k is given by

$$\phi^k_{n,S}(S) = \begin{cases} a^k + (b^k - a^k)(S - S^k_a)/(S^k_b - S^k_a) & \text{if } S \in \left]S^k_a, S^k_b\right[\\ 0 & \text{otherwise} \end{cases} \,, \tag{8}$$

where the size variable s is characterized here by the surface S of the droplets. Three different cases may be encountered within a given section as depicted in Fig. 3, the four parameters a^k, b^k, S_a^k and S_b^k depending on both time and position, unlike the sections' lower and upper bounds s_{k-1} and s_k which are predetermined and unchanged through the entire computation process.

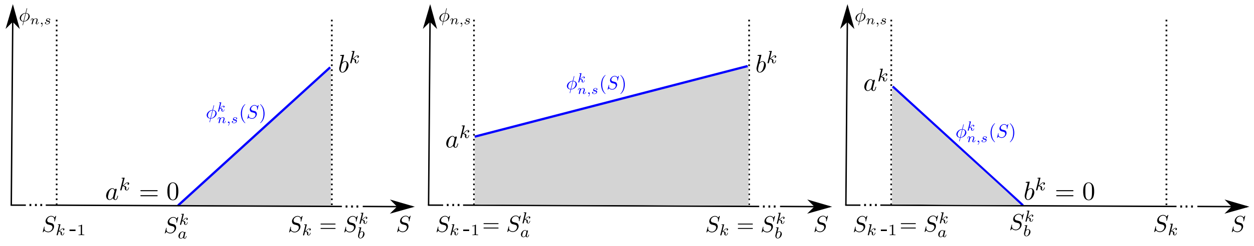

Figure 3: Shape of the affine-TSM reconstruction within one section of the particle size distribution [27, 28].

Finally, thanks to a mathematical derivation of the WBKE (7) not reproduced here (see [42, 45]), and in the framework of the sectional approach described above, one can obtain the following system of Eulerian equations written in vector form for the dispersed phase:

$$\partial_t \boldsymbol{\mathcal{Q}}^k \;+\; \nabla.\left(\boldsymbol{\mathcal{Q}}^k \otimes \boldsymbol{v}^k\right) \;=\; \boldsymbol{\mathcal{S}}^k\,, \quad k \in [\![1, N_s]\!] \quad . \tag{9}$$

In this system, $\boldsymbol{\mathcal{Q}}^k = (\rho^k \quad \rho^k \boldsymbol{v}^k \quad \rho^k e^k \quad n^k)^t$ is the vector of the transported moments of the NDF for a given section k, namely the bulk mass density, the momentum, the internal energy and the number density, $\boldsymbol{v}^k$ and e^k being respectively the velocity vector and the specific internal energy, while $\boldsymbol{\mathcal{S}}^k$ may include any relevant source term for the configuration to be treated, as detailed in the next section. The corresponding primitive variables $\boldsymbol{u}^k = (\alpha^k \quad \boldsymbol{v}^k \quad \theta^k \quad D^k)^t$ are the volume fraction and mean velocity, temperature and diameter of the section. They are bijectively related to the transported moments according to

$$\alpha^k = \frac{\rho^k}{\rho_0\left(\theta^k\right)}\,, \quad \boldsymbol{v}^k = \frac{\rho^k\,\boldsymbol{v}^k}{\rho^k}\,, \quad D^k = \left(\frac{6\alpha^k}{\pi n^k}\right)^{1/3}\,, \quad e^k = e_{ref} + \int_{\theta_{ref}}^{\theta^k} c_v(\theta^k)\,\mathrm{d}\theta^k\,, \tag{10}$$

where $\rho_0\left(\theta^k\right)$ and $c_v\left(\theta^k\right)$ are the density and specific heat capacity of the pure liquid medium, both depending on the droplets temperature θ^k, while e_{ref} is the internal energy at a reference temperature θ_{ref}. Note that according to its above definition from the volume fraction and the number density, the mean diameter D^k is actually a volume mean diameter (D_{30}). Also note that by definition, the particle number density n^k is directly related to the integral of the particle number size distribution in section k:

$$n^k = \int_{S_{k-1}}^{S_k} \phi^k_{n,S}(S)\,\mathrm{d}S\,. \tag{11}$$

Another relation links the bulk mass density ρ^k to an equivalent integral form of the particle number size distribution, namely

$$\rho^k = \frac{\rho_0\left(\theta^k\right)}{6\sqrt{\pi}} \int_{S_{k-1}}^{S_k} S^{3/2} \phi^k_{n,S}(S)\,\mathrm{d}S\,. \tag{12}$$

In practice, this means that whenever necessary (for instance when evaluating the source terms), the four affine-TSM parameters a^k, b^k, S_a^k and S_b^k can be obtained from n^k and ρ^k, and vice versa (see details about the numerical inversion procedure given by Doisneau [46] for instance).

To conclude, let us make a comment on the fact that the mean droplet diameter D^k can be actually comparable or even larger than the size of the mesh elements in practical simulations, such as the one presented in section 4. Indeed, one might wonder how the DPS approach handles it. It must be kept in mind that the modeling of the dispersed phase is primarily based on a statistical description, namely the WBKE giving the evolution of the NDF in the phase space. The mesh resolution is nothing else than the discretization of some particular dimensions of the phase space, namely that of the physical space. Using a very fine mesh size, potentially smaller than the particle diameter, is therefore not problematic. The combined data of a mean droplet diameter D^k and a number density n^k in a given mesh cell of volume V_c must be interpreted as the probability of finding, at a given time t, a spray whose mean diameter is D^k in that volume V_c, regardless of its size. More detailed information on these statistical considerations can be found e.g. in [5, 47, 48].

2.4. Coupled system of equations and source terms

The coupled system of equations for both SPS and DPS can be finally written in vector form as

$$\left\{\begin{array}{lll} \partial_t \boldsymbol{Q} & + \nabla.\,(\boldsymbol{F} - \boldsymbol{\varphi}) & = \boldsymbol{G} + \boldsymbol{L} + \boldsymbol{C} \\ \partial_t \boldsymbol{\mathcal{Q}}^k & + \nabla.\,(\boldsymbol{\mathcal{Q}}^k \otimes \boldsymbol{v}^k) & = \boldsymbol{\mathcal{G}}^k + \boldsymbol{\mathcal{L}}^k + \boldsymbol{\mathcal{B}}^k + \boldsymbol{\mathcal{E}}^k \ , \quad k \in [\![1, N_s]\!] \end{array}\right. , \tag{13}$$

where it is recalled that $\boldsymbol{Q}$ and $\boldsymbol{\mathcal{Q}}^k$ denote the conservative variables in the SPS and in the DPS respectively, $\boldsymbol{F}$ and $\boldsymbol{\varphi}$ are the convective and diffusive fluxes in the SPS, while N_s is the number of sections used in the DPS to discretize the droplet size distribution. In system (13) above, the source terms $\boldsymbol{S}$ and $\boldsymbol{\mathcal{S}}^k$ have been recast according to the phenomena involved in the envisioned applications, which means at least primary atomization and secondary break-up, evaporation and combustion reactions. Thus, the source terms are broken down as follows:

- $\boldsymbol{G} = \left(G_{M_1} \ \ldots \ G_{M_{N_g}} \ 0 \ G_V \ G_E\right)^t$ and $\boldsymbol{\mathcal{G}}^k = \left(\mathcal{G}_M^k \ \mathcal{G}_V^k \ \mathcal{G}_E^k \ \mathcal{G}_N^k\right)^t$ comprise the mass, momentum and heat exchange source terms **between the gas phase and the spray**. Regarding applications in the field of LRE, these exchange terms are mostly due to drag force, evaporation and heating, for which state-of-the-art models are available in the literature. Furthermore, when considering evaporation as the only mass transfer between the dispersed phase and the gas phase, source terms in both solvers are related to one another according to:

$$G_{M_v} = -\sum_{k=1}^{N_s} \mathcal{G}_M^k \ , \quad G_{M_i} = 0 \quad \text{if } i \neq v \ , \quad G_V = -\sum_{k=1}^{N_s} \mathcal{G}_V^k \ , \quad G_E = -\sum_{k=1}^{N_s} \left(\mathcal{G}_E^k + X_g^k\right) \ , \tag{14}$$

where the index v refers to the vapor species within the gas mixture (for example gaseous oxygen in the case of LOX droplets). Besides, X_g^k gathers additional terms that arise in the SPS but are not present in the DPS, because the former solves an equation on the total energy whereas the latter solves an equation on the internal energy only. These additional terms include for instance the work of body forces and the transfer of kinetic energy associated to the evaporation mass transfer.

- $\boldsymbol{L} = (0 \ \dots \ 0 \ L_M \ L_V \ L_E)^t$ and $\boldsymbol{\mathcal{L}}^k = \left(\mathcal{L}_M^k \ \mathcal{L}_V^k \ \mathcal{L}_E^k \ \mathcal{L}_N^k\right)^t$ gather the mass, momentum and heat exchange source terms **between the dense liquid phase and the spray**, which are linked together as follows:
$$L_M = -\sum_{k=1}^{N_s} \mathcal{L}_M^k \ , \quad L_V = -\sum_{k=1}^{N_s} \mathcal{L}_V^k \ , \quad L_E = -\sum_{k=1}^{N_s} \left(\mathcal{L}_E^k + X_l^k\right) \ , \tag{15}$$
X_l^k containing the additional terms due to the total energy formulation in the SPS. These exchanges may occur both ways: from the SPS to the DPS they stand for the primary atomization of the dense liquid core, while from the DPS to the SPS they are due to the impingement of liquid droplets onto the dense liquid core. The modeling of these source terms is a novel contribution within the overall strategy proposed in this paper, and as such will be exposed specifically in section 3.

- $\boldsymbol{C} = \left(\dot{\omega}_1 \ \dots \ \dot{\omega}_{N_g} \ \ 0 \ \ 0 \ \ 0\right)^t$ includes the **combustion reaction source terms** which potentially concern all gaseous species in the SPS, and whose modeling must be adapted to the actual combustion regime. See for instance the modeling adopted in section 4 for the simulation of the Mascotte configuration.

- $\boldsymbol{\mathcal{B}}^k = \left(\mathcal{B}_M^k \ \mathcal{B}_V^k \ \mathcal{B}_E^k \ \mathcal{B}_N^k\right)^t$ contains exchange source terms between the current section k and potentially all other sections, due to **secondary break-up** [49]. Indeed, droplets belonging to any superior section are prone to break-up into smaller droplets whose size fall into the range of section k, while droplets of section k may also break-up into smaller droplets belonging to any inferior section.

- $\boldsymbol{\mathcal{E}}^k = \left(\mathcal{E}_M^k \ \mathcal{E}_V^k \ \mathcal{E}_E^k \ \mathcal{E}_N^k\right)^t$ gathers exchange source terms between consecutive sections only, resulting from the **evaporation** process that make the size distribution move towards increasingly smaller sizes [28].

In the sectional formalism, the effective computation of any source term related to the spray evaporation or break-up involves the following procedure:

(i) select an appropriate model describing the phenomenon at the scale of one single isolated droplet,

(ii) as soon as this model depends on the droplet size, integrate the source term expression over the size interval of each section k (this may be done either analytically or numerically),

(iii) use dedicated robust and efficient schemes for the numerical integration of the source term. This issue has been addressed in the works of Sibra et al. [28] and Dufour [50].

Note that integrating the size-dependent source terms over each size section requires the prior computation of the coefficients S_a^k, S_b^k, a^k and b^k which define the number size distribution $\phi_{n,S}^k$ in the affine-TSM method, as previously explained. Incidentally, an interesting feature of the affine-TSM reconstruction when compared to other sectional reconstructions is that it facilitates the evaluation of size-integrated source terms, in particular by enabling analytical computations of some integrals [27, 28].

3. Primary atomization modeling

3.1. Recasting of the liquid-liquid coupling source terms

As described in Table 1, the source terms $\boldsymbol{L}$ and $\boldsymbol{\mathcal{L}}^k$ related to the coupling between the dense liquid phase and the spray are first broken down into two separate contributions, each one corresponding to a one-way transfer only:

- terms with index A refer to a transfer strictly from the liquid phase in the SPS towards the dispersed phase in the DPS, which indicates the actual **primary atomization** phenomenon.
- terms with index C refer to a transfer strictly in the opposite way, namely from the dispersed phase in the DPS towards the liquid phase in the SPS. This is to account for the possible **coalescence** of droplets with the dense liquid phase[1], which may occur for instance when the liquid core is flapping and captures droplets on its way, or because droplets are trapped in vortices that make them impinge onto the liquid core.

Hence, the mass transfer terms with indices $_{M_A}$ and $_{M_C}$ in Table 1 are nonnegative by definition. Also note that $X_l^k = X_{l_A}^k - X_{l_C}^k$ includes the additional energy terms arising in the SPS due to the total energy formulation, as previously explained in section 2.4.

Only some of the terms in Table 1 need to be modeled, the other ones being easily inferred afterwards from conservation principles. Indeed, as illustrated in Fig. 4, a modeling is required for L_{M_A}, the primary atomization mass flow rate in the SPS. Together with a modeling for the properties of the atomized droplets (for instance in terms of mean diameter D_A, velocity $\boldsymbol{v}_A$ and temperature θ_A), one can then deduce $\mathcal{L}_{M_A}^k$, the atomization mass flow rates dispatched accross the sections of the DPS, as well as $\mathcal{L}_{V_A}^k$, $\mathcal{L}_{E_A}^k$ and $\mathcal{L}_{N_A}^k$, the contributions to the momentum, internal energy and number density equations of each section, and eventually L_{V_A} and L_{E_A}, the corresponding terms in the momentum and total energy equations of the SPS. Similarly, a modeling is required for $\mathcal{L}_{M_C}^k$, the coalescence mass flow rate in a given section of the DPS.

---

[1] Not to be confused with the coalescence between droplets, which is not considered in the present paper.

Table 1: Recasting of the liquid-liquid coupling source terms.

	Net flux		Atomization	Coalescence		
DPS	$\mathcal{L}^k_M$	$=$	$+\ \mathcal{L}^k_{M_A}$	$-\ \mathcal{L}^k_{M_C}$		
	$\mathcal{L}^k_V$	$=$	$+\ \mathcal{L}^k_{V_A}$	$-\ \mathcal{L}^k_{V_C}$		
	$\mathcal{L}^k_E$	$=$	$+\ \mathcal{L}^k_{E_A}$	$-\ \mathcal{L}^k_{E_C}$		
	$\mathcal{L}^k_N$	$=$	$+\ \mathcal{L}^k_{N_A}$	$-\ \mathcal{L}^k_{N_C}$		
SPS	L_M	$=$	$-\ L_{M_A}$	$+\ L_{M_C}$		
		$=$	$-\ \sum_k \mathcal{L}^k_{M_A}$	$+\ \sum_k \mathcal{L}^k_{M_C}$	$=$	$-\ \sum_k \mathcal{L}^k_M$
	L_V	$=$	$-\ L_{V_A}$	$+\ L_{V_C}$		
		$=$	$-\ \sum_k \mathcal{L}^k_{V_A}$	$+\ \sum_k \mathcal{L}^k_{V_C}$	$=$	$-\ \sum_k \mathcal{L}^k_V$
	L_E	$=$	$-\ L_{E_A}$	$+\ L_{E_C}$		
		$=$	$-\ \sum_k \left(\mathcal{L}^k_{E_A} + X^k_{l_A}\right)$	$+\ \sum_k \left(\mathcal{L}^k_{E_C} + X^k_{l_C}\right)$	$=$	$-\ \sum_k \left(\mathcal{L}^k_E + X^k_l\right)$

Combined with the properties of the spray in that section (D^k, $\boldsymbol{v}^k$ and θ^k), which are transported quantities, this provides $\mathcal{L}^k_{V_C}$, $\mathcal{L}^k_{E_C}$ and $\mathcal{L}^k_{N_C}$, the contributions to the momentum, internal energy and number density equations of each section, as well as L_{M_C}, L_{V_C} and L_{E_C}, the respective source terms in the SPS.

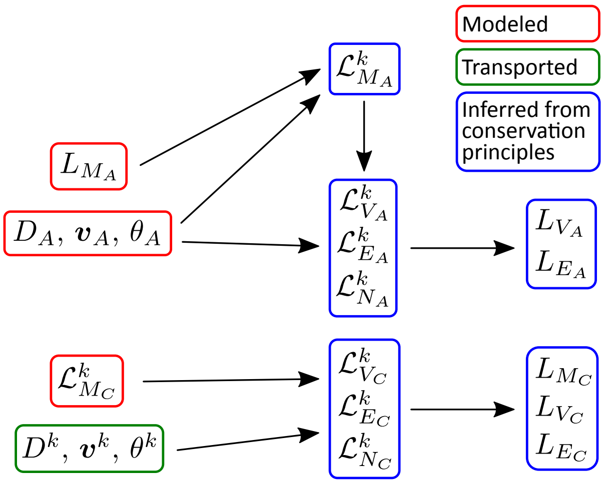

Figure 4: Layout of the computation procedure of liquid-liquid coupling source terms. (Color online.)

3.2. Modeling of the primary atomization mass flow rate and properties of the atomized droplets

The modeling proposed for the primary atomization mass flow rate L_{M_A} reads in

$$L_{M_A} = \rho Y_l f_A \lambda_A \ , \tag{16}$$

where f_A is a characteristic frequency, which has to be primarily related to the local velocity difference between both phases, as this is what mainly drives the atomization process downstream of coaxial injectors. This information is unfortunately not available in the homogeneous mixture model, comprising only one mean velocity. However the local velocity gradient can still be used as an estimate, for instance by means of the turbulent frequency f_T. The latter is classically defined in the context of compressible LES as [24]:

$$f_T = (2\boldsymbol{D}{:}\boldsymbol{D})^{1/2} \ , \tag{17}$$

with $\boldsymbol{D}$ the deviator of the resolved symmetric strain rate tensor. This deviator reads

$$\boldsymbol{D} = \frac{1}{2}\left[\boldsymbol{\nabla} \otimes \boldsymbol{u} + (\boldsymbol{\nabla} \otimes \boldsymbol{u})^t\right] - \frac{1}{3}(\boldsymbol{\nabla} \cdot \boldsymbol{u})\boldsymbol{I}_3 \ , \tag{18}$$

with $(\boldsymbol{\nabla} \otimes \boldsymbol{u})^t$ the velocity gradient tensor. The atomization characteristic frequency f_A is thus supposed to be directly related to this turbulent frequency f_T, which simply means here that we take $f_A = f_T$.

Moreover, $\lambda_A = 1 - \tanh\left(4Y_l^2\right)$ is an activation function whose shape has been chosen in a pragmatic and empirical way, so as to localize the interface, as this is where primary atomization is likely to occur, but also for numerical stability reasons. Indeed, it is important that the transfer operates on the gaseous side of the diffuse interface, i.e. in mesh elements in which the volume occupied by the liquid in the SPS is negligible. Otherwise the low compressibility of the liquid would bring about significant spurious pressure oscillations.

Once transferred to the DPS, the liquid phase is supposed to be in the form of spherical droplets. Ideally, an appropriate modeling based on the local flow features should provide the properties of these atomized droplets, for instance in the form of their local mean diameter D_A, velocity $\boldsymbol{v}_A$ and temperature θ_A. However, such a modeling seems out of reach within the framework of the homogeneous mixture diffuse interface model, which provides no information on the local disequilibria between both phases. Consequently, this issue has not been addressed yet, which means that case-specific uniform values have to be assumed for each simulation (see section 4). Assuming then that D_A, $\boldsymbol{v}_A$ and θ_A are constant throughout a given entire computation, one can easily derive the other source terms. With only one possible value of the diameter D_A, then the mass transfer from the SPS is inevitably operated towards only one single section of the DPS, which is on top of that the last one (comprising the biggest diameters), i.e. such that $k = N_s$. Indeed, when coalescence between droplets is not considered, the droplet size is maximum just after primary atomization and can only decrease afterwards due to break-up and evaporation. Therefore one can write:

$$k < N_s \begin{cases} \mathcal{L}^k_{M_A} &= 0 \\ \mathcal{L}^k_{V_A} &= 0 \\ \mathcal{L}^k_{E_A} &= 0 \\ \mathcal{L}^k_{N_A} &= 0 \end{cases} , \qquad k = N_s \begin{cases} \mathcal{L}^k_{M_A} &= L_{M_A} \\ \mathcal{L}^k_{V_A} &= \mathcal{L}^k_{M_A}\, \boldsymbol{v}_A \\ \mathcal{L}^k_{E_A} &= \mathcal{L}^k_{M_A}\, e(\theta_A) \\ \mathcal{L}^k_{N_A} &= \mathcal{L}^k_{M_A} \,/\, m\,(D_A, \theta_A) \end{cases} , \tag{19}$$

where $m(D_A, \theta_A) = \rho_0(\theta_A)\, \pi D_A^3/6$ is the mass of one droplet of diameter D_A and temperature θ_A. In the same way as for the section mean diameters D^k, D_A has to be interpreted as the volume mean diameter (D_{30}) of the atomized droplets. Finally, L_{V_A} and L_{E_A} can be straightforwadly obtained as exposed in Table 1.

3.3. Modeling of the coalescence mass flow rate

The modeling proposed for the coalescence mass flow rate $\mathcal{L}^k_{M_C}$ reads in

$$\mathcal{L}^k_{M_C} = \rho^k f_C \lambda^k_C \,, \tag{20}$$

with $f_C = (N_C \Delta t)^{-1}$ a characteristic frequency, Δt the simulation time step and N_C a relaxation parameter. Note that the rate at which the impingement occurs at the subgrid scale level should be rigorously modelled. However, the main purpose of this impingement source term is to avoid having spray in the dense core, otherwise leading to modeling peculiarities (like liquid droplets surrounded by a purely liquid carrier phase, which would make no sense). Therefore, capturing the accurate dynamics of the impingement mechanism is not of major importance as long as we make sure that no droplets can cross the diffuse interface zone towards the liquid core without being transfered to the SPS. This is why f_C is here a numerical frequency but not a physical one. The activation function is expressed as $\lambda^k_C = 1 - \tanh\left(-2 \log \alpha_l\right)$, with α_l the liquid phase volume fraction in the SPS, defined by Eq. (6). In the same way as for the function λ_A, its shape has been chosen for practical reasons, namely to make sure that the transfer be operated when the liquid volume fraction in the SPS is high, indicating the vicinity of dense liquid.

From D^k, $\boldsymbol{v}^k$ and θ^k, the properties of the spray in section k, one can easily derive afterwards the corresponding source terms in the momentum, total energy and number density equations. These are given by

$$1 \le k \le N_s \begin{cases} \mathcal{L}^k_{V_C} &= \mathcal{L}^k_{M_C}\, \boldsymbol{v}^k \\ \mathcal{L}^k_{E_C} &= \mathcal{L}^k_{M_C}\, e(\theta^k) \\ \mathcal{L}^k_{N_C} &= \mathcal{L}^k_{M_C} \,/\, m\,(D^k, \theta^k) \end{cases} , \tag{21}$$

where $m(D^k, \theta^k) = \rho_0(\theta^k)\, \pi {D^k}^3/6$ is the mass of one droplet of diameter D^k and temperature θ^k. Furthermore, L_{M_C}, L_{V_C} and L_{E_C}, the opposite source terms in the SPS, are obtained as sums of the above source terms on all sections, as written in Table 1.

4. Simulation of a cryogenic subcritical flame

4.1. Parameters and numerical methods

In order to evaluate the ability of the numerical strategy to deal with cryogenic rocket engine operating conditions, it has been applied to the simulation of the A10 fire test on the Mascotte test bench, documented in [51–53]. The chamber is a 458 mm-long tube closed by an axisymmetric nozzle. A single coaxial injector is used to inject LOX through the central tube and GH_2 through the annular tube. Helium is injected through two rows of holes in order to protect side windows against hot gas flow inside the chamber. Geometric specifications are given in Fig. 5. The chamber pressure of 10 bar implies subcritical conditions for injected LOX. Mass flow rates and temperatures are respectively $50\,\mathrm{g\,s^{-1}}$ and 85 K for LOX, $23.7\,\mathrm{g\,s^{-1}}$ and 280 K for GH_2 and $10\,\mathrm{g\,s^{-1}}$ and 280 K for He, which gives a mixture ratio around 2 and a momentum ratio around 15. The simulation is performed on a 3D mesh of the full chamber geometry, from the injector to the nozzle outlet. The mesh is made up of 9.8 million cells, 19.6 million faces and 1.7 million vertices. Except for prism layers near the walls of the injectors, all mesh cells are tetrahedral elements. Fig. 5 shows the mesh in the upstream half part of the chamber, in the vicinity of the injector, where $D_l = 5\,\mathrm{mm}$ is the LOX post diameter at the injector exit. On this figure, Δ stands for the averaged value of $6V/A$, where V is the cell volume and A is the total area of the cell faces. For regular tetrahedra, this parameter corresponds to the circumscribed sphere diameter. Inside the injector and along $8D_l$, a box is meshed with an averaged element size Δ_1 chosen in order to meet certain criteria. First, the mesh must be able to capture the biggest liquid structures downstream the liquid core, but also the main instabilities propagating at its surface due to shear stresses and resulting in its atomization. In the particular conditions simulated in this paper, the physical analysis proposed by Marmottant and Villermaux [54] predicts wavelengths for longitudinal and tranverse instabilities of $\lambda_{/\!/} = 2.5\,\mathrm{mm}$ and $\lambda_{\perp} = 250\,\mu\mathrm{m}$ respectively. Secondly, it is generally accepted that at least 80 % of the turbulent kinetic energy must be resolved when dealing with LES [55]. In this case, the ratio between the cell size Δ and the integral scale length L_t is estimated by $\Delta/L_t = 0.083$. When applying this criterion to the LOX post, for which L_t can be estimated as the diameter upstream the post chamfer $D_i = 3.6\,\mathrm{mm}$, the maximum suitable cell size appears to be $\Delta = 300\,\mu\mathrm{m}$. As concerns the annular coaxial duct, L_t can be estimated as the thickness of the channel $e = 3.2\,\mathrm{mm}$, leading to a maximum suitable cell size of $\Delta = 270\,\mu\mathrm{m}$. To comply with these three conditions, the averaged element size Δ_1 is set to $100\,\mu\mathrm{m}$. In addition, two tetrahedra are considered along the $300\,\mu\mathrm{m}$ injector lip thickness. As seen in Fig. 5, two other boxes are meshed with averaged element sizes Δ_2 and Δ_3 respectively, also set to resolve at least 80 % of the turbulent kinetic energy. In their work, Ko and Au [56] state that eddies formed upstream in the gaseous co-current flow around the liquid jet join beyond a certain distance to form a fully-merged jet. According to the authors, this *reattachment point* is located at a distance of approximately 5 to $6D_g$ (or equivalently 12 to $15D_l$ in the present study) from the injection plane, whatever the mean velocity ratio. On the basis of this observation, it is then possible to consider that the biggest vortices downstream the reattachment point have a size included between the external annular channel diameter $D_g = 12\,\mathrm{mm}$ and the height of the chamber $h = 50\,\mathrm{mm}$. This leads to a maximum suitable cell size of $\Delta = 1\,\mathrm{mm}$ to $\Delta = 4\,\mathrm{mm}$. As a result, Δ_2 and Δ_3 are set to averaged values of $500\,\mu\mathrm{m}$ and $1.5\,\mathrm{mm}$ respectively. Finally, the downstream half of the chamber, not shown in Fig. 5 and starting from $40D_l$, is a coarse region with 3 mm-high elements. As for boundary conditions, inlet mass flows and associated temperatures are imposed at injector inlets, 10 mm upstream the injection plane. Adiabatic no-slip condition is imposed at chamber and injector walls.

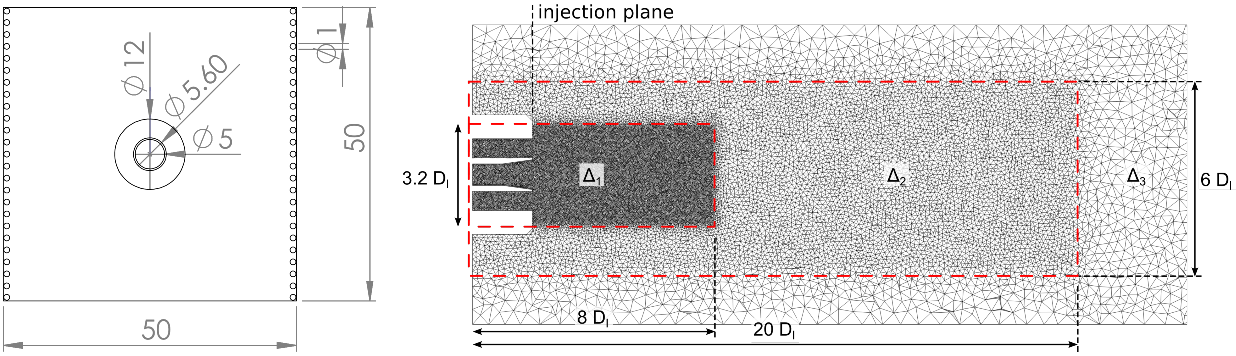

Figure 5: Left: front view of the injection plane (dimensions in mm); Right: mesh cut in the median plane.

Regarding numerical methods, both solvers use a cell-centered Finite Volume approach on general unstructured meshes. They also use upwind numerical schemes, namely the classical HLLC scheme of Toro et al. [57] for the SPS and a Godunov-like scheme for the DPS, adapted to the weak hyperbolicity of the system. These numerical fluxes are computed from reconstructed values at the faces centroids, which are obtained by means of the multislope MUSCL method developed in a previous work [58]. This is a second-order accurate and robust reconstruction method, adapted to general unstructured meshes, able to cope with the strong gradients, high density ratios and discontinuous solutions inherent to two-phase flow simulations. As exposed by Buffard and Clain [59], the principle of multislope methods is to compute the reconstructed values on the faces by an appropriate combination of backward and upward scalar slopes relative to each face, by means of limitation procedures inherited from the classical monodimensional MUSCL technique of van Leer [60]. Furthermore, an operator splitting technique is used with dedicated second-order time-stepping schemes for each operator, either explicit for the coupling source terms operator and the convective operator of the DPS, or implicit for the convective operator of the SPS.

After reaching steady-state conditions, the calculation was averaged over 17 ms of physical time, which was sufficient to compute about 7 convective times of the dense LOX core and 2.5 convective times of burnt gases along the whole chamber. This computation stage required 900 000 hCPU on Intel Ivy Bridge processors, with typical runs involving 500 to 1500 MPI processes. It is worth noting that this quite large CPU cost is mainly due to the low amplitude of LOX injection velocity, and to the large total length of the chamber. Because of these two characteristics, a considerable physical time had to be computed in order to converge time averages.

4.2. Physical modeling

As previously explained in section 2.4, classical state-of-the-art models are selected to describe the physical phenomena acting at the scale of a single LOX droplet. Thus, Schiller and Naumann's correlation [61] accounts for the drag force, and Abramzon and Sirignano's model [62] is used to describe evaporation and heating. When computing the evaporation mass flow rate, we need to calculate some properties of the liquid-vapor equilibrium, such as $P_{vap}(T)$ and $l_{vap}(T)$, the equilibrium vapor pressure and latent heat of vaporization at a given temperature T, or $T_{sat}(P)$ the saturation temperature (boiling point) at a given pressure P. These properties are obtained by classical correlations, such as the Antoine equation:

$$\ln P_{vap} = A - \frac{B}{T+C} \,, \tag{22}$$

$$T_{sat} = \frac{B}{A \ln P} - C \,, \tag{23}$$

$$l_{vap} = \alpha \left(1 - \frac{T}{T_c}\right)^{\beta} \,, \tag{24}$$

where T_c is the temperature at the critical point, whereas A, B, C, α and β are parameters depending on the substance. In the case of oxygen, these parameters have the following values: $T_c = 154.58\,\mathrm{K}$, $A = 20.662$, $B = 787.247$, $C = -4.00948$, $\alpha = 291342$ and $\beta = 0.3608$. This evaporation modeling is then converted so as to comply with the sectional formalism, especially by allowing fluxes between consecutive sections, as described in [27, 28].

In the same way, secondary break-up is rendered by means of coupling source terms between all sections of the size distribution. Their formulation in the sectional formalism is due to Dufour et al. [49], from Pilch and Erdman's modeling of the break-up time of a single droplet [63], and Wert's model for the mean size of the resulting fragments [64]. Primary atomization is modeled as explained in section 3, with properties of the atomized droplets postulated from the physical analysis proposed by Marmottant and Villermaux [54]. That gives for the mean diameter and velocity: $D_A = 250\,\mu\mathrm{m}$ and $||\boldsymbol{v}_A|| = 16\,\mathrm{m\,s^{-1}}$ with the direction of $\boldsymbol{v}_A$ being that of $\boldsymbol{u}$, the local velocity vector in the SPS. For the configuration adressed in this study, in which the liquid-phase flow is surrounded by a high-velocity coflow, simple test cases have shown that the drag force induced by the gaseous coflow on liquid droplets rapidly changes the size and velocity distributions of the spray, mainly by the secondary break-up phenomenon. Then the results presented below are weakly dependent on the values chosen for D_A and $\boldsymbol{v}_A$, provided that they have the good order of magnitude, estimated by the physical analysis mentionned above. The droplet temperature θ_A is assumed to be that of the LOX at the injector inlet. The spray size distribution is discretized into $N_s = 3$ sections, as this number appeared sufficient to ensure a good statistical convergence in terms of mean spray diameter. Section upper bounds are respectively 40 μm, 120 μm and 280 μm. They were chosen based on the expected distribution shape: the last one is chosen close to the mean diameter of atomized droplets, as they are not allowed to grow further, whereas the first one is chosen sufficiently small to well describe the numerous droplets resulting from secondary break-up and evaporation. Due to a very high injection Weber number (higher than 10^4), the surface tension can be considered negligible at the resolved scales, and no model is then used. In addition, an implicit LES approach is adopted for this simulation. Note that this is not an inherent feature of the coupling framework introduced in this paper. The latter is just waiting to be improved with appropriate subgrid turbulent dissipation models accounting for compressible two-phase flows effects. However, this is a work on its own (see e.g. [29]), that has been left to future works.

In high-pressure cryogenic H_2-O_2 flames, chemical reactions can be assumed to be faster than other processes due to the high reactivity of pure hydrogen [65]. A simple time-scale combustion model, similar to [66, 67], is then used. Chemical species are supposed to relax towards local chemical equilibrium with a time scale linked to the driving process, i.e. turbulent mixing. Gas species reaction source terms then write

$$\dot{\omega}_i = \begin{cases} \min\left(f_C, f_M\right) \rho \left(Y_i^{\mathrm{eq}}(Z) - Y_i\right) & \text{if } T > T_{\mathrm{inf}} \\ 0 \text{ otherwise,} \end{cases} \tag{25}$$

where f_C, the characteristic frequency of the chemical reaction in the assumption of infinitely fast chemistry, is supposed to be driven by the turbulent frequency f_T defined by equation (17). This means that $f_C = C f_T$, where $C = 1.5$ is a model parameter. In addition, $f_M = 10^5\,\mathrm{s}^{-1}$ is a limit frequency to prevent overestimation of reaction rates in highly strained regions for specific applications, $Y_i^{\mathrm{eq}}(Z)$ the equilibrium mass-fraction of species i computed at the local mixture fraction Z at fixed enthalpy and pressure, Y_i the local mass fraction of species i and $T_{\mathrm{inf}} = 350\,\mathrm{K}$ a limit temperature of inflammability. In order to recover proper thermodynamic conditions in the chamber, the minimum set of six species (H_2, GO_2, H_2O, OH, H, O) was considered [68]. The heat release rate $\dot{\omega}_T$ can be computed according to

$$\dot{\omega}_T = \sum_{i=1}^{N_g} \dot{\omega}_i \Delta H_{f_i}^0 \,, \tag{26}$$

where $\Delta H_{f_i}^0$ are the enthalpies of formation of the N_g gas species. More details regarding the physical properties used for the different chemical species are given in Appendix A.

The choice of the main parameters of the combustion model, namely C and f_M, is expected to have a limited impact on the results for the configuration simulated in this study. First, because combustion mostly takes place in the propellant mixing layer, where the turbulent frequency is sufficiently high to entail reaction source terms that are limited by locally available amount of reactants rather than by the characteristic frequency f_C. Secondly, because H_2/O_2 combustion is known as extremely fast combustion. In such conditions, the turbulent characteristic time will always remain higher than the combustion one, and the value of f_M is chosen in such a way that it does not have any influence on reaction source terms.

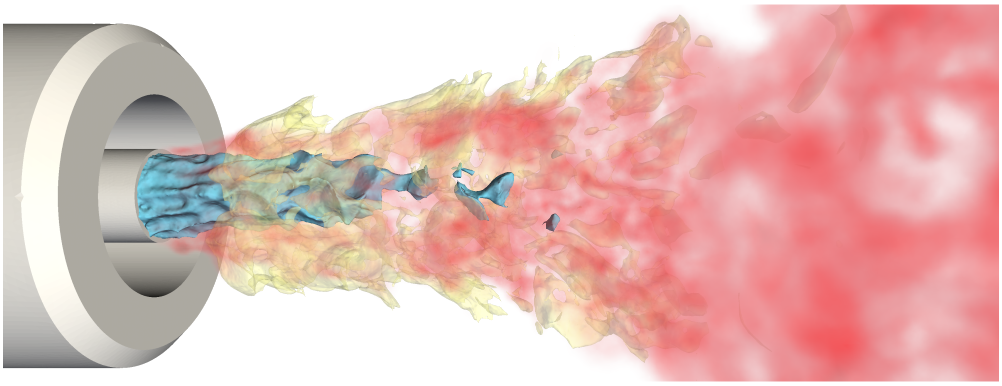

Figure 6: Isocontours of dense phase volume fraction (blue), heat release rate (yellow) and volume rendering of spray phase volume fraction (red). (Color online.)

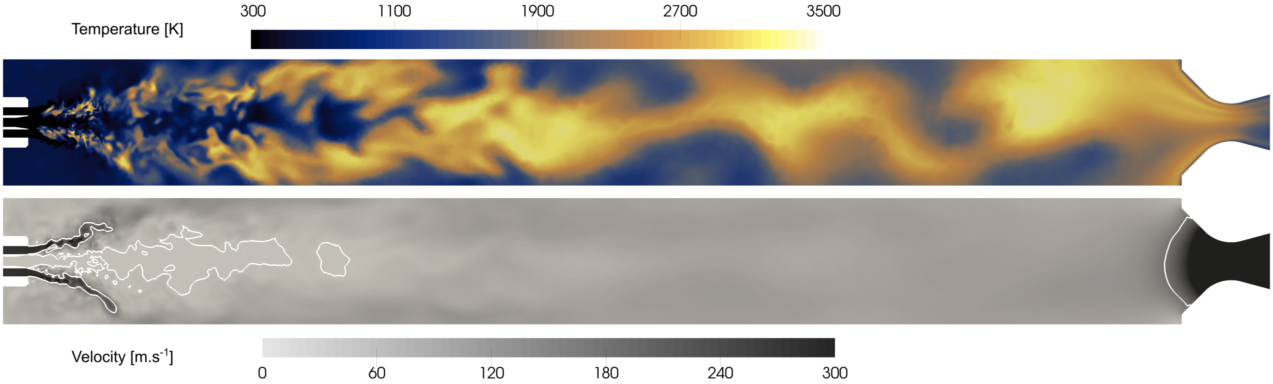

Figure 7: LOX reactive jet in the MASCOTTE chamber: vertical center plane coloured by temperature on the top picture, and by velocity on the bottom picture, and velocity isocontours at $10\,\mathrm{m\,s^{-1}}$ and $150\,\mathrm{m\,s^{-1}}$. (Color online.)

To conclude, it is worth noting that both the implicit LES approach and the combustion model used here are not state-of-the-art, however they can be replaced by any other, more refined models. The present work focuses on the coupling and overall integration, not on the individual components. As a first realistic attempt to use the numerical strategy proposed in this work, models were primarily chosen for their robustness.

4.3. Simulation results

4.3.1. Overall flow dynamics

A snapshot of the LOX flow is shown in Fig. 6: the dense LOX core is highlighted by an isosurface of liquid volume fraction ($\alpha_l = 0.5$) resulting from the SPS. It is strongly convoluted because of the shear with the fast hydrogen flow and large chunks of liquid are detached at the tip of the dense core. The spray of LOX droplets, created by the atomization model from the dense phase, is represented by a volume rendering of the volume fraction of the dispersed phase computed by the DPS (all sections considered). This cloud of droplets surrounds the dense core as a thin layer close to the injector lip. It then forms a larger cloud further downstream under gas-phase driving force, which is surrounded by the flame represented by an isosurface of heat release rate ($\dot{\omega}_T = 8 \times 10^{10}\,\mathrm{W\,m^{-3}}$). Figure 7 shows a longitudinal cut of instantaneous temperature and velocity fields. A layer of burnt gases is sandwiched between the LOX core and the fuel stream. Further downstream, large pockets of burnt gases are convected to the nozzle. Regarding the velocity field, it is typical of coaxial injectors with a slow central jet surrounded by a fast stream, which expands radially because of the heat release. Figure 8 shows the dense core near the injector, together with H_2 and GO_2 mass fractions and an isocontour of heat release rate at $2 \times 10^{10}\,\mathrm{W\,m^{-3}}$. Oxygen vapor is created very close to the injector lip by means of the atomization of dense LOX and evaporation of LOX spray droplets. These phenomena occur in the high turbulent-level mixing layer between LOX jet and H_2 coaxial jet. It highlights the quite low characteristic time associated to this chain of phenomena. Despite the presence of gaseous oxygen near the injector lip, the main heat release rate area is located at almost one injector-diameter length downstream, that indicates a lifted flame. As evaporation of the dense liquid phase is neglected in this study, oxygen vapor concentration may be underestimated in this particular area where liquid droplets are convected downstream before completely evaporating. A specific dense phase evaporation model could bring the lacking oxygen concentration needed to allow the flame to stabilize on the injector lip. Such a model, potentially based on the interface area density at subgrid level, remains to be formulated for the specific case of assisted coaxial atomization (see e.g. the recent work of [32] that brings a contribution to that effort). In addition, the grid size may affect the resolution of large-scale vortices in this particular area, leading to a bias on residence times of gas and droplets and preventing the flame from going upstream.

To go further in describing the liquid phase, Fig. 9 shows the LOX mass fraction field with two isolines of the net atomization rate defined as $L_M = L_{M_C} - L_{M_A}$, namely an isoline of positive net atomization rate $L_M = 1000\,\mathrm{kg\,m^{-3}\,s^{-1}}$, and an isoline of negative net atomization rate $L_M = -1000\,\mathrm{kg\,m^{-3}\,s^{-1}}$. The atomization area ($L_M < 0$) is seen to be located in the diffused interface area where the LOX mass fraction is sufficiently low. This is due to the combination of activation function λ_A and frequency f_A which are part of the atomization mass rate (see eq. (16)). As for the reverse transfer ($L_M > 0$), namely coalescence, it takes place at the dense core rim, enabling the droplets not to be trapped by the liquid core flappening. It would be interesting to analyze in more details the effect of this coalescence term, for instance by running extra simulations with this term deactivated, but this is a task that goes beyond the scope of the present paper. The net atomization mass transfer, as well as the associated momentum and energy transfers, lead to the formation of a spray whose volume fraction fields are represented in Fig. 10 for each section, together with an isoline of evaporation rate at $5000\,\mathrm{kg\,m^{-3}\,s^{-1}}$.

Several notable zones can be highlighted. Close to the injector, inside the mixing layer, droplets of section 1 (diameter smaller than $40\,\mu$m) appear dominant in volume. In this area, the turbulent shear intensity is sufficient to mostly transfer droplets of section 3 to section 1 under secondary break-up effect. From $2D_l$ downstream the injector, shear intensity decreases and secondary break-up feeds section 1 and 2. Further downstream, as diffuse interface thickness increases, secondary break-up intensity decreases and droplets stay in section 3. Areas of strong evaporation, located in Fig. 10 thanks to the isoline, are correlated with the presence of droplets of section 1 that induce a high evaporation surface area. They lead to the presence of oxygen vapor as highlighted in Fig. 8.

In addition, the fields related to the liquid phase in Fig. 9 and 10 can be compared to shadow imaging acquisitions of Fdida et al. [69] for similar operating conditions (see e.g. Fig. 7 in [69]). Although shadow imaging does not discriminate between liquid core and small droplets, at least without involving dedicated image processing, it can be observed that the topology of the whole liquid-phase flow depicted on experimental images is similar to that of the whole liquid-phase flow numerically simulated, namely the overlay of the dense phase mass fraction and the volume fraction of spray droplets. In both numerical and experimental images, it can be seen that the liquid-gaz interface is highly wrinkled by the surrounding flame and gaseous coflow. Moreover, when going downstream the liquid phase flow expands radially, while ejecting small droplets.

4.3.2. Spray dynamics

In order to better quantify the droplets repartition across the sections, one can easily compute the local number size distribution $\phi^k_{n,S}(S)$ from ρ^k and n^k, the mass and number density of section k in any given mesh element, as explained in 2.3 and thoroughly described by Laurent et al. [27]. To provide more useful information on the overall flow features, this distribution can be expressed in diameter variable rather than surface variable

$$\phi^k_{n,D}(D) = \frac{dS}{dD}\phi^k_{n,S}(S) = 2\pi D \phi^k_{n,S}(S)\,, \tag{27}$$

then translated to a volume size distribution

$$\phi^k_{v,D}(D) = \frac{\pi (D^k)^3}{6}\phi^k_{n,D}(D)\,, \tag{28}$$

namely the volume fraction occupied by all droplets of diameter D (expressed in $\mathrm{m}^3\,\mathrm{m}^{-3}\,\mathrm{m}^{-1}$), and finally averaged over space (i.e. over some set of mesh elements). Note that when expressed in diameter rather than surface, the distribution is obviously not affine anymore. Thus, Fig. 11 plots the volume size distribution of each spray section, expressed in diameter variable and computed by means of space averaged ρ^k and n^k, namely over four transverse layers of thickness $2D_l$ along the injector axis, as well as over the full chamber volume. These distributions are computed from an instantaneous field during the steady-state regime, namely the same as that depicted in Fig. 8–10. Compared to Fig. 10, same trends can be observed: in layer $[0, 2D_l]$, section 1 is predominantly populated due to high secondary break-up, compared to sections 2 and 3. These latter are more and more populated as the distance from the injector increases. All considered distributions show a similar shape: section 1 ($[0, 40\,\mu\mathrm{m}[$) and section 2 ($[40\,\mu\mathrm{m}, 120\,\mu\mathrm{m}[$) contain droplets resulting from secondary break-up and evaporation, while section 3 ($[120\,\mu\mathrm{m}, 280\,\mu\mathrm{m}[$) shows a larger distribution shape that results from primary atomization at a $250\,\mu$m D_{30} diameter. The same idea remains for the full chamber spray where, for this instant picture, sections 1 and 2 involve nearly $20\,\%$ of spray volume (or mass) whereas $80\,\%$ are involved in section 3.

Note that the shape of the volume size distributions shown in Fig. 11 cannot be compared directly to the experimental ones. This is due to the particular assumptions made for the shape of the numerical distribution in each section (affine in surface variable), which tends to generate a discontinuous overall distribution when the number of sections is low. A way to improve the overall shape of the distribution, and make it converge towards a more representative droplet size distribution, is therefore to increase the number of sections, as shown in [27]. However, the number of three sections here is a good compromise between the simulation cost and a minimal discretization of the size space making it possible to describe the evolution of the mean spray features under the effect of evaporation and break-up in the sectional framework.

4.3.3. Liquid core dynamics

The numerical strategy proposed here is able to retrieve the dynamic behavior of both dense core and spray. To illustrate this, Fig. 12 plots the time evolution of the length of the intact liquid core normalized by the LOX post diameter D_l. The growth-and-detachment behavior experimentally observed by Hardi et al. [13] is qualitatively retrieved: successive drops of intact core length result from the shedding of large-scale LOX structures. Low frequency growths of intact core length are also observed (e.g. for $t \in [59, 61\,\mathrm{ms}]$), that suggests that occasional events may shift local flow conditions from the average. In order to provide a quantitative validation of the intact core length obtained in the simulation, it is planned in a future work to perform detailed comparisons with experimental measurements. Such measurements already exist for cryogenic oxygen at various subcritical and supercritical operating points (see for example the work of Hardi et al. [13] and Fdida et al. [70]), but unfortunately not yet for the operating point of the MASCOTTE test bench that has been simulated in this paper. Besides, comparisons with theoretical correlations is another interesting way of validation, as there are a number of these available in the literature [71–74]. However, as pointed out by Fdida et al. [70], all these correlations were developed from cold flow data, which means that they should be handled carefully in a reactive context. Indeed, the flow conditions in the liquid core area might then be significantly different from the conditions at injection due to the presence of the surrounding flame. Furthermore, Xiao et al. [75] emphasized that such correlations cannot be unified because the intact core length depends on the turbulence characteristics of the flow inside the injector. By comparing LES results of a water/air coaxial jet simulated with either laminar or turbulent inlet boundary conditions, these authors showed that such effect is important for Weber numbers less than 1000, for the specific coaxial injector simulated in their study. They assessed their numerical methodology by simulating a liquid jet in coaxial air flow well documented by Charalampous et al. [76]. They retrieved Weber number and momentum flux ratio dependences of intact core lentgh consistent with existing experimental measurements.

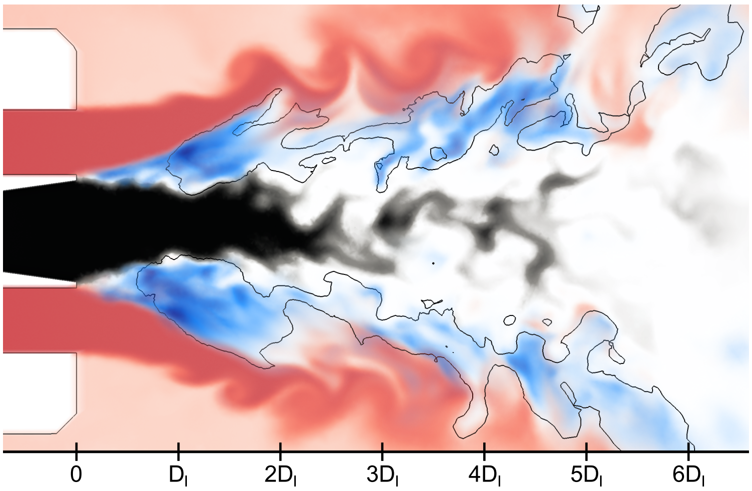

Figure 8: Instantaneous near-field cut of the median plane colored by dense phase volume fraction (white: 0; black: 1), GO_2 mass fraction (white: 0; blue: 1), H_2 mass fraction (white: 0; red: 1) and isocontour of heat release rate at $2 \times 10^{10}\,\mathrm{W\,m^{-3}}$ (black). (Color online.)

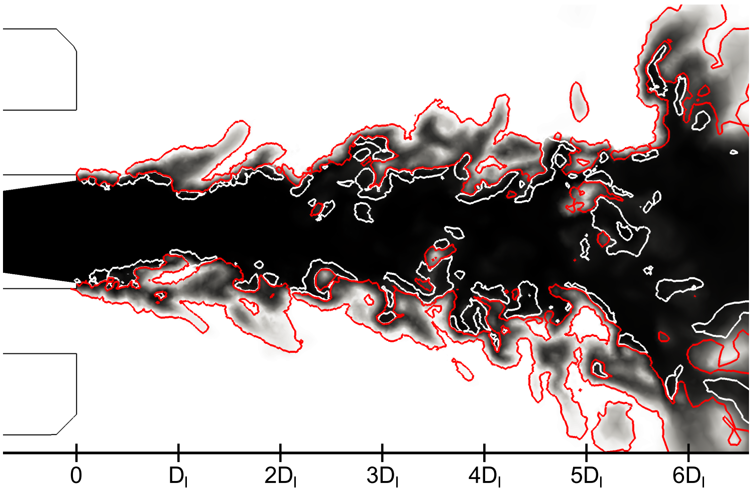

Figure 9: Instantaneous near-field cut of the median plane colored by dense phase mass fraction (greyscale) with isolines of positive net atomization rate at $L_M = 1000\,\mathrm{kg\,m^{-3}\,s^{-1}}$ (white) and negative net atomization rate at $L_M = -1000\,\mathrm{kg\,m^{-3}\,s^{-1}}$ (red). (Color online.)

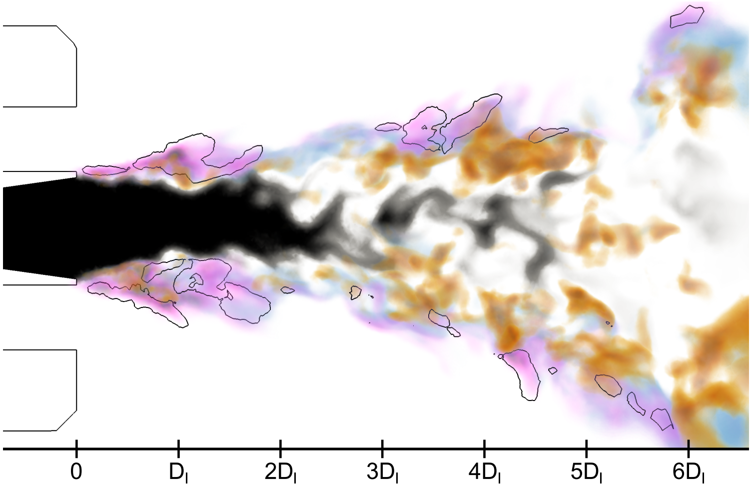

Figure 10: Instantaneous near-field cut of the median plane colored by dense phase volume fraction (greyscale) and droplet volume fractions of sections 1 to 3 (pink, blue, brown resp.), with an isoline of evaporation rate at 5000 kg m^{-3} s^{-1} (black). (Color online.)

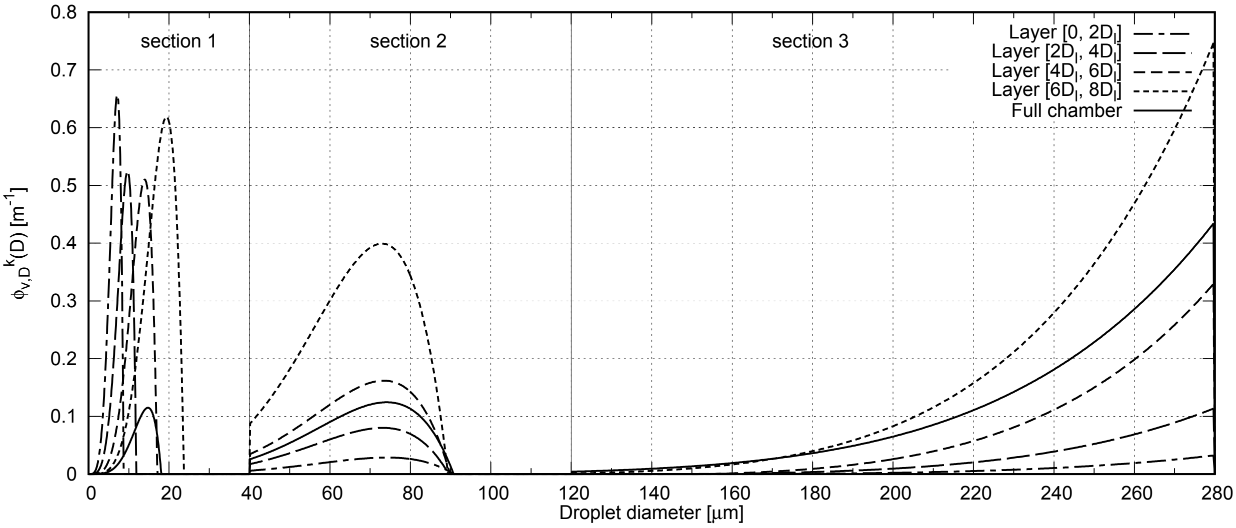

Figure 11: Volume size distribution of liquid droplet diameter, inside four transverse layers.

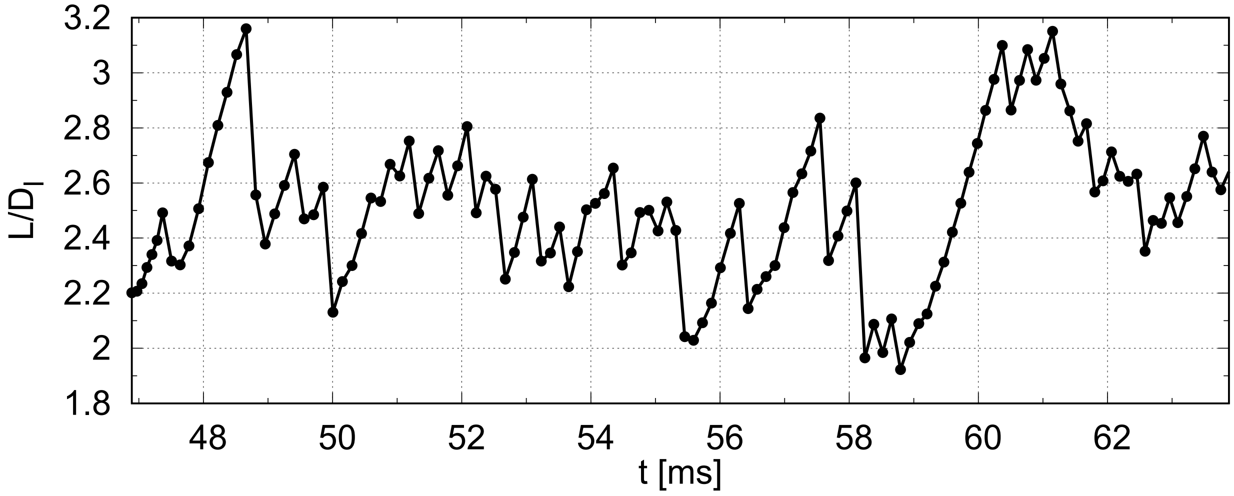

Figure 12: Time evolution of normalized intact core length, measured from the liquid volume fraction isosurface of 0.99 (—●—).

This important validation step remains to be completed in higher Weber number and momentum ratio conditions to get closer to rocket engine flows.

In the recent work of [77], which applies the numerical strategy introduced in this paper to a non-reactive simulation, the intact core length is found to be in very good agreement with the theoretical correlation of [71]. This result is an important first step in the validation process of the overall strategy, and offers promising prospects. Indeed, as the liquid core behavior is known to be coupled with unsteady combustion, it is able to induce the growth of HF combustion instabilities [13]. Hence, the proposed strategy appears to be a relevant framework to address this issue in the future.

4.3.4. Comparison with experimental data

Analyzing mean temperature fields is a good way to assess the reliability of the whole methodology. Figure 13 shows a longitudinal cut of the mean temperature field evaluated from a 17 ms time average. The presence of the LOX dense core is revealed by the cold area along the injector axis up to $15D_l$. Further downstream, between $25D_l$ and $60D_l$, the hotest area mainly results from progressive turbulent mixing between combustion products and remaining hydrogen that induces heat release until reaching thermodynamic equilibrium. Coherent Anti-Stokes Raman Spectroscopy (CARS) measurements were acquired by Grisch et al. [78] at three axial locations in the chamber, shown in Fig. 13. Temperatures deduced from H_2 and H_2O CARS measurements are compared to simulation mean temperature profiles in Fig. 14. Error bars designate uncertainties estimated to be about 10 % of measured temperature, and validation rates in % indicate the ratio between the number of usable measurements and the total number of laser shots. For the sake of clarity, only measurements with a validation rate above 25 % were reported from [78]. The radial shape of the three temperature profiles is well retrieved, revealing that, upstream (at $10D_l$ and $20D_l$), combustion occurs in the mixing zone between reactants, far from the centerline, and downstream (at $40D_l$), it expands

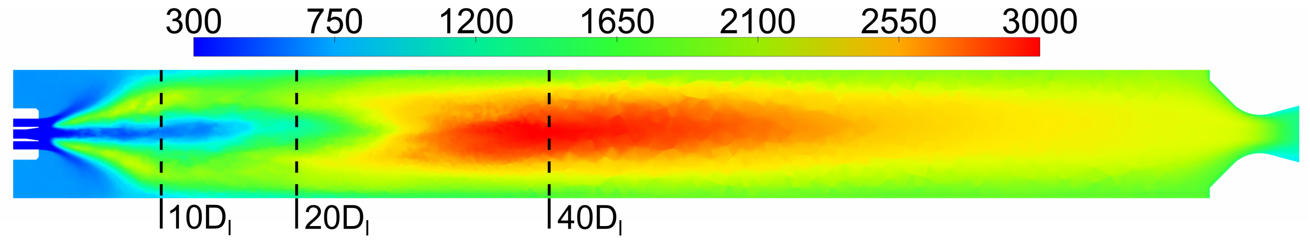

Figure 13: Mean temperature field on the center plane [K] and axial locations of CARS measurements. (Color online.)

into a more homogeneous flow under the effect of turbulent mixing. The qualitative agreement in shape of the temperature profiles suggests that the flame shape and length is fairly well predicted by CFD. However, there are still some discrepancies between numerical and experimental temperature profiles, especially at $10D_l$. This area is among those where the temperature fluctuations have the highest amplitude. This is due to the successive presence of cold propellants and hot burnt gases in a zone where the mixing is imperfect but the combustion is strong. This is not only seen in the simulation but also in the experiment. As a result, this brings about rather high uncertainties on the experimental measurements, as revealed by the quite low validation rates given in Fig. 14 at $10D_l$. On the other hand, these fluctuations are also difficult to capture very accurately with CFD. This is mainly due to the numerical dissipation (at $10D_l$ we are not in the finest mesh zone anymore as depicted in Fig. 5) and the lack of a proper modeling of the subgrid turbulent dissipation. These combined effects may explain the discrepancies between the numerical and experimental temperature profiles, especially at the location $10D_l$.

An insight on LOX spray characteristics is proposed by comparing simulation results with Phase Doppler Particle Analysis (PDPA) measurements realized by Gicquel and Vingert [79] on the MASCOTTE test bench for the same operating point. During the simulation, diameter and volume fraction of droplets were acquired for each section, at each timestep and at the exact locations of measurements. With these data, statistical diameters of the time averaged distributions were finally computed to be compared to statistical diameters evaluated on each experimental sample. Figure 15 plots Sauter mean diameters at each measurement location along the radial coordinate at two axial position ($6D_l$ and $10D_l$) from the injector outlet plane. Simulation discrepancies are about 50 % at $6D_l$ whereas the agreement is far better at $10D_l$. It is worth noting that such comparison is not straightforward because PDPA was set to measure droplet diameters between 14.3 μm and 500 μm, whereas in the DPS, the droplet size space was discretized between 0 and 280 μm. As illustrated in Fig. 10 and 11, smallest droplets seem to be preferentially located upstream, whereas biggest droplets increasingly prevail downstream. That may induce a bias on diameter comparison especially at $x = 6D_l$ if smallest droplets are not taken into account by PDPA whereas they are considered in the simulation. Anyhow, the methodology presented in this paper seems to describe the LOX spray with physically relevant diameters. A dedicated study of validation of primary atomization modeling, with recent measurement data [80], is an ongoing work that remains compulsory to assess its reliability.

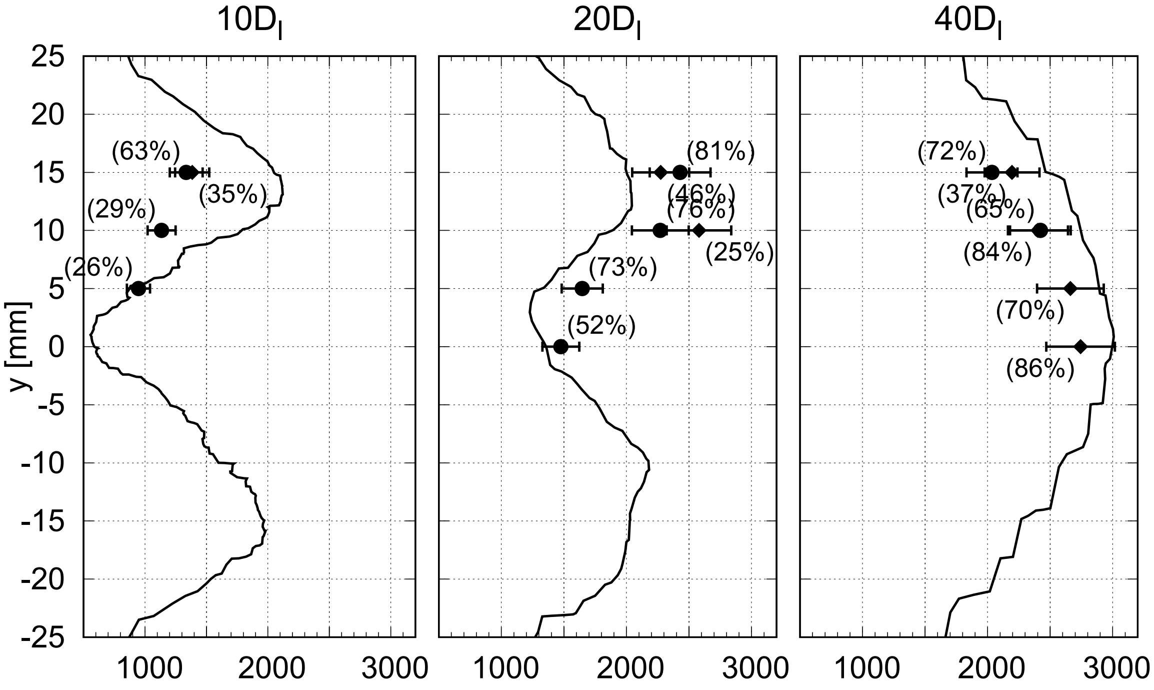

Figure 14: Mean temperature transverse profiles [K] (—) and CARS measurements based on H_2 (◆) and H_2O (●) with associated validation rates in %.

4.3.5. Evaluation of the mesh influence

The spatial discretization is a key parameter of the presented methodology, as the thickness of the liquid-gaz interface rendered by the diffuse interface model strongly depends on the size of the mesh cells. The flow hydrodynamics also depends on the mesh size, especially in the mixing layer between propellants where the smallest vortices just downstream the injector lip need a sufficiently fine mesh to be accurately captured. Based on the physical criteria given in section 4.1, the mesh used in this study was considered sufficient to obtain overall results weakly dependent on the mesh size, and then relevant to demonstrate the ability of the numerical methodology to reproduce cryogenic reactive two-phase flows. To assess this statement quantitatively, two additional simulations were performed in the same conditions with two different meshes derived from the original M0 mesh, previously described in section 4.1. Mesh M1 is an intermediary mesh with Δ_1 and Δ_2 multiplied by 1.5 from the M0 values, whereas mesh M2 is a coarse one with Δ_1 muliplied by 3 and Δ_2 multiplied by 2 from the M0 values. The initial state of these two simulations was the M0 simulation state at $t = 46.8\,\text{ms}$, i.e. the starting time of Fig. 12 and of the time-averaged computation window. Figure 16 compares the time evolution of the liquid core length for these two simulations with the original one. As expected, the grid size has a direct effect on the dense liquid-phase description. A coarser mesh tends to increase the numerical diffusion of the liquid volume fraction field. In that case, the intact core length, characterized from a given liquid volume fraction value, therefore decreases. Results on mesh

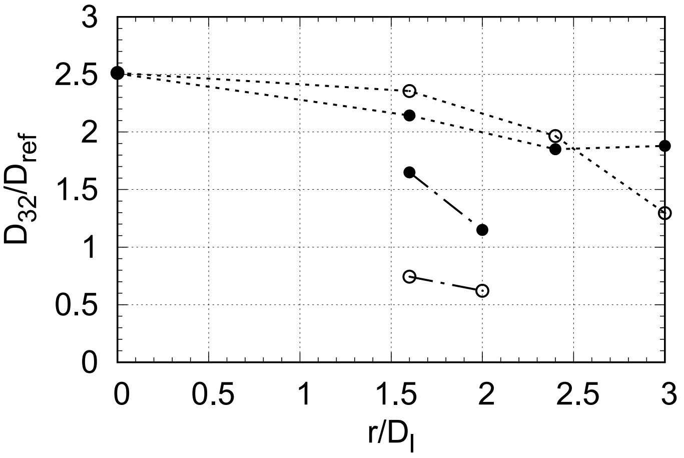

Figure 15: Reduced Sauter mean diameters from experimental measurements (●) and simulation results (○), at $6D_l$ from the injection plane (—·—·) and $10D_l$ (- - - - -).

M2 show such a behavior, whereas on mesh M1 the liquid core length remains similar in average to the one on mesh M0. Its dynamic behavior is different from the M0 simulation because mesh refinement also affects the gas flow description around the liquid phase, and preferentially in the area of smallest vortices, just downstream the injector lip, which is also where the instabilities of the liquid-gas interface are triggered.

For this latter reason, grid-size effects also appear significant when comparing time-averaged temperature profiles, plotted in Fig. 17. The averaged temperature field is highly dependent on the mesh, particularly upstream in the chamber. As combustion in such configuration is driven by the mixing between propellants, discretization of vortices in the mixing layer is a key parameter for the overall flow features. As a result, the mesh convergence cannot be demonstrated with the tested meshes. This would require the use of finer meshes, unfortunately associated to highly time-consuming simulations. Nevertheless, section 4.3.4 has shown that the mesh M0 is sufficient to obtain quite good comparisons between numerical results and experimental data.

5. Conclusion

In this paper, a simulation and modeling strategy has been proposed to describe the whole chain of mechanisms involved in cryogenic injection under subcritical operating conditions, from primary atomization to combustion. In this strategy, particular attention has been paid to model the dynamics of the dense liquid atomization process under aerodynamic constraints. For this purpose, a coupling between a homogeneous diffuse interface model for the dense liquid phase and a kinetic-based Eulerian model accounting for the liquid dispersed phase is proposed. This coupling is based on a mass transfer between both models which is adapted to the modeling of primary atomization in the framework of coaxial TPF. The new strategy has

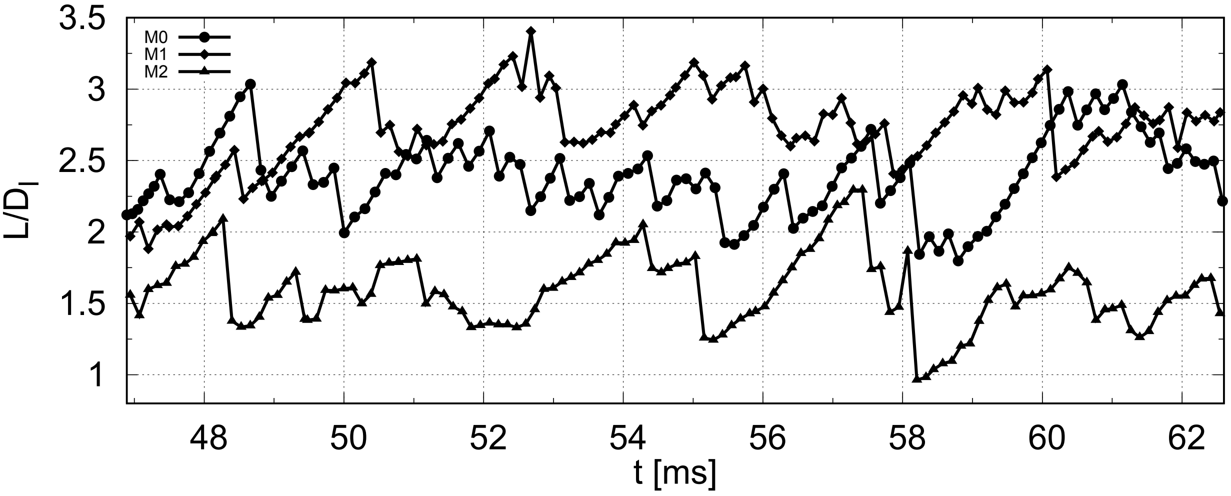

Figure 16: Time evolution of normalized intact core length, measured from the liquid volume fraction isosurface of 0.99, for the three mesh cases.

been successfully applied to the unsteady simulation of a cryogenic flame in subcritical conditions.

Thanks to this strategy, the LOX dense core dynamics has been retrieved, showing a highly convoluted dense flow and high-frequency break-ups. The atomized spray has been described with a size distribution discretized into three sections, subjected to mass transfer due to atomization, evaporation and secondary break-up phenomena. Comparisons with experimental results have shown that the flame shape and Sauter mean diameters of the spray are well reproduced by the simulation. This study provides a promising framework to study the onset, growth and sustaining of high-frequency combustion instabilities in LRE, as well as in any other application field involving primary atomization in a reactive context. As an example, the strategy proposed in this paper has been used recently by Rutard et al. [77] to study the atomization of an air-assisted liquid jet under a high-frequency transverse acoustic forcing.

The present paper focuses on demonstrating the capacity of the strategy to simulate realistic cryogenic flows. To go on, future work is still necessary to gradually improve each part of the strategy, and get an accurate, validated and robust numerical tool. As previously stated, the modeling of subgrid turbulent dissipation and turbulent combustion shall be improved, and validated in the context of cryogenic combustion. This forthcoming comprehensive validation of the models will rely on the experimental campaigns performed on the Onera's Mascotte test bench in the last few years and still currently in progress. Similarly, the atomization model proposed in this study was a first simple attempt to model such a complex phenomenon. Future work will contribute to assess its degree of accuracy and improve its formulation in a more complex and less empirical way. Indeed, considering uniform values for the properties of the created droplets after atomization could be a limiting feature of the current strategy, as it could lead to an inaccurate estimation of the spray dynamics and evaporation, and consequently of the flame behavior. Neglecting the evaporation mass transfer in the SPS might also be a limitation, as a substantial amount of liquid mass might then

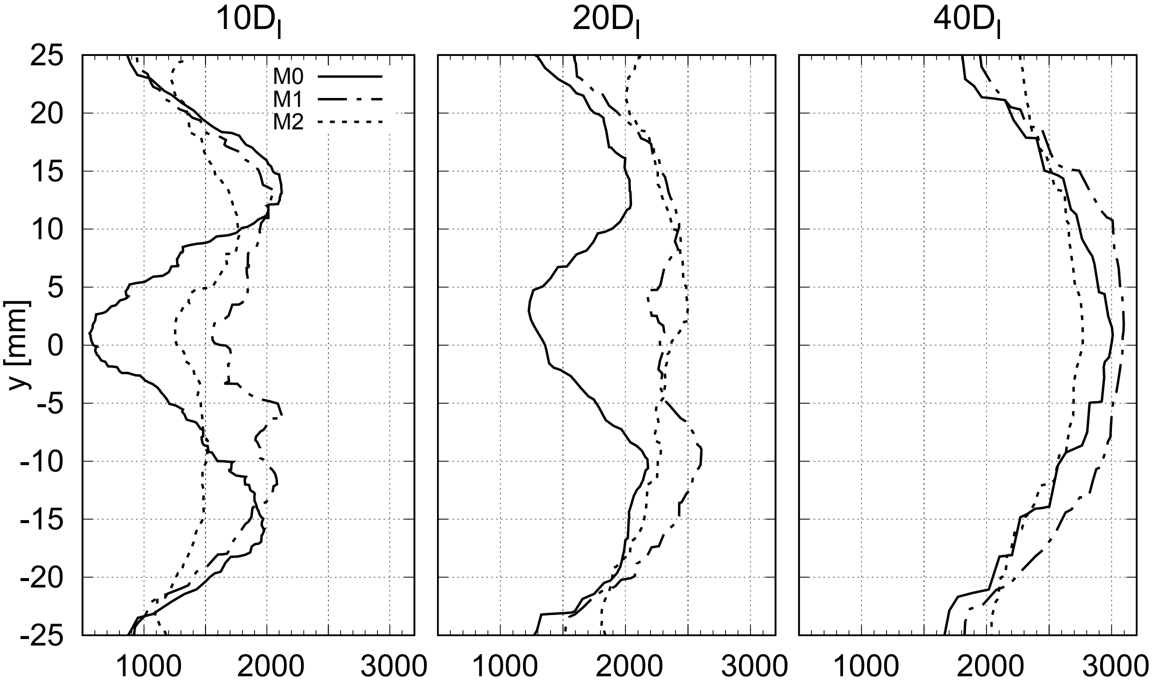

Figure 17: Mean temperature transverse profiles [K] for original mesh (———), mesh M1 (— - — -) and M2 (- - - - - - -).

not be converted into droplets, and therefore not transfered to the DPS. With no proper evaporation mass transfer in the SPS, the total amount of vaporized oxidizer (or fuel depending on the application) required to feed the combustion could therefore be insufficient.

One way of improvement could lie in a subgrid modeling of the interface topology, e.g. by means of a transport equation for the surface density area, with closure source terms adapted to the LES context (see e.g. [24]). Another promising way is to adapt the strategy to a more detailed diffuse interface model, giving locally access e.g. to the temperature and the velocity of each phase, as well as to some geometrical variables combined with the surface density area, thereby providing a thorough description of the interface topology at the subgrid scale level (see for instance the ongoing work of [38–40]). This should enable a more accurate modeling of the droplets properties after primary atomization, and more generally extend the scope of applicability of the proposed methodology.

Regarding the spray modeling, it would be interesting to perform simulations with an increased number of sections to discretize the droplet size distribution, so that the shape of the overall distribution be more comparable to real experimental distributions. Thus, it would be interesting to analyse to what extent this increased level of accuracy regarding the spray polydispersion has a noticeable impact on the overall results, for instance in terms of the flame behaviour.

Acknowledgments

This work was supported by a PhD grant from Onera – The French Aerospace Lab, and performed using HPC resources from GENCI-TGCC (Grant 2015-t20152b7502). The authors would like to thank Dr. Nicolas Fdida for helpful discussions on the experimental diagnostics performed on the Mascotte test bench.

Appendix A. Physical properties of the chemical species in the Mascotte simulation

This appendix provides the modeling elements used for the physical properties of the chemical species in the simulation of the Mascotte test bench presented in section 4.

Gas species

The isobaric molar heat capacity of each species is modeled by a polynomial in temperature, according to classical fitting methods (see for example [81]):

$$\widetilde{c_p}(T) = \sum_{k=0}^{n} a_k (T/T_{sc})^k \ , \tag{A.1}$$

where $T_{sc} = 1000\,\mathrm{K}$ is a scaling parameter. The values of the $n+1$ polynomial coefficients a_k for each gaseous species used in the simulation are given in Table A.2. The viscosity of each gaseous species is modeled by the Sutherland's law [82]:

$$\mu(T) = \mu_0 \left(\frac{T}{T_0}\right)^{3/2} \frac{T_0 + T_1}{T + T_1} \ , \tag{A.2}$$

where the values of the parameters μ_0, T_0 and T_1 are given in Table A.2. The thermal conductivity of each gaseous species is modeled by the Eucken's law, which can be expressed as:

$$\lambda(T) = \mu(T) \left[\frac{\widetilde{c_p}(T)}{W} + \frac{5R}{4W}\right] \tag{A.3}$$

where W is the molar mass of the species, and R is the ideal gas constant. The enthalpy of formation ΔH_f^0 of each gaseous species is given in Table A.2 at the reference state $P_{ref} = 1\,\mathrm{bar}$ and $T_{ref} = 298.15\,\mathrm{K}$.

Liquid species

A constant value of $\widetilde{c_p} = 53.8\,\mathrm{J\,mol^{-1}\,K^{-1}}$ is assumed for the isobaric molar heat capacity of the LOX species (the only one liquid species considered in the simulation), as well as a constant value of $\mu = 2.45 \times 10^{-4}\,\mathrm{Pa\,s}$ for its viscosity. The thermal conductivity of the LOX is fitted by a linear function of temperature:

$$\lambda(T) = \max\left(\lambda_{min}, \lambda_A + \lambda_B T\right) \ , \tag{A.4}$$

with $\lambda_{min} = 2 \times 10^{-2}\,\mathrm{W\,m^{-1}\,K^{-1}}$, $\lambda_A = 2.816 \times 10^{-1}\,\mathrm{W\,m^{-1}\,K^{-1}}$ and $\lambda_B = -1.45 \times 10^{-3}\,\mathrm{W\,m^{-1}\,K^{-2}}$. For a reference state $P_{ref} = 10\,\mathrm{bar}$ and $T_{ref} = 85\,\mathrm{K}$, we have the isothermal compressibility of the LOX

Table A.2: Physical properties of the gaseous species.

Species	ΔH_f^0 $\left[\mathrm{kJ\,mol^{-1}}\right]$	$\widetilde{c_p}(T)$ - polynomial coefficients $\left[\mathrm{J\,mol^{-1}\,K^{-1}}\right]$				Viscosity		
		a_0	a_1	a_2	a_3	μ_0 [μPa s]	T_0 [K]	T_1 [K]
		a_4	a_5	a_6	a_7			
H	218.00	20.786	0	0	0	7.4800	300	123.48
		0	0	0	0			
H_2	0	15.645	96.255	−258.63	345.70	8.9700	300	179.38
		250.18	100.65	−21.189	1.8196			
H_2O	−241.83	31.677	8.7441	−16.929	44.248	12.280	373.20	1048.5
		−41.264	18.579	−4.1403	0.367 09			
He	6.2194	20.800	−0.128 48	0.385 83	−0.549 03	19.930	300	156.78
		0.419 09	−0.176 19	0.038 431	−0.003 396			
O	249.18	25.361	−19.675	37.513	−39.144	20.540	300	248.44
		23.800	−8.4045	1.5973	−0.126 22			
O_2 (gas)	0	30.350	−18.509	75.504	−97.762	20.740	300	175.53
		64.680	−23.470	4.4531	−0.346 15			
OH	37.278	35.320	−35.509	81.161	−95.252	44.830	1000	899.61
		67.068	−27.528	6.0016	−0.534 68			

$\beta_0 = 2.58 \times 10^{-9}\,\mathrm{Pa^{-1}}$, the reference density $\rho_0 = 1178\,\mathrm{kg\,m^{-3}}$ and the enthalpy of formation $\Delta H_f^0 = -15.239\,\mathrm{kJ\,mol^{-1}}$.

References

[1] B. Franzelli, A. Vié, M. Boileau, B. Fiorina, N. Darabiha, Large Eddy Simulation of Swirled Spray Flame Using Detailed and Tabulated Chemical Descriptions, Flow, Turbulence and Combustion 98 (2017) 633–661. URL: `https://doi.org/10.1007/s10494-016-9763-0`. doi:`10.1007/s10494-016-9763-0`.

[2] R. Lebas, T. Menard, P. Beau, A. Berlemont, F. Demoulin, Numerical simulation of primary break-up and atomization: DNS and modelling study, International Journal of Multiphase Flow 35 (2009) 247–260. URL: `http://linkinghub.elsevier.com/retrieve/pii/S0301932208001821`. doi:`10.1016/j.ijmultiphaseflow.2008.11.005`.

[3] F. Doisneau, M. Arienti, J. Oefelein, On Multi-Fluid models for spray-resolved LES of reacting jets, Proceedings of the Combustion Institute 36 (2017) 2441 – 2450. URL: `http://www.sciencedirect.com/science/article/pii/S1540748916303789`. doi:`https://doi.org/10.1016/j.proci.2016.07.120`.

[4] L. Hakim, A. Ruiz, T. Schmitt, M. Boileau, G. Staffelbach, S. Ducruix, B. Cuenot, S. Candel, Large eddy simulations of multiple transcritical coaxial flames submitted to a high-frequency transverse acoustic modulation, Proceedings of the Combustion Institute 35 (2015) 1461 – 1468. URL: `http://www.sciencedirect.com/science/article/pii/S154074891400145X`. doi:`https://doi.org/10.1016/j.proci.2014.05.142`.

[5] S. Jay, F. Lacas, S. Candel, Combined surface density concepts for dense spray combustion, Combustion and

Flame 144 (2006) 558–577. URL: `http://linkinghub.elsevier.com/retrieve/pii/S0010218005002531`. doi:`10.1016/j.combustflame.2005.07.017`.

[6] T. Poinsot, Prediction and control of combustion instabilities in real engines, Proceedings of the Combustion Institute 36 (2017) 1 – 28. URL: `http://www.sciencedirect.com/science/article/pii/S1540748916300074`. doi:`https://doi.org/10.1016/j.proci.2016.05.007`.

[7] M. E. Harvazinski, W. E. Anderson, C. L. Merkle, Analysis of Self-Excited Combustion Instabilities Using Two- and Three-Dimensional Simulations, Journal of Propulsion and Power 29 (2013) 396–409. URL: `https://doi.org/10.2514/1.B34732`. doi:`10.2514/1.B34732`.

[8] L. Selle, R. Blouquin, M. Théron, L.-H. Dorey, M. Schmid, W. Anderson, Prediction and Analysis of Combustion Instabilities in a Model Rocket Engine, Journal of Propulsion and Power 30 (2014) 978–990. URL: `http://dx.doi.org/10.2514/1.B35146`. doi:`10.2514/1.B35146`.

[9] A. Urbano, Q. Douasbin, L. Selle, G. Staffelbach, B. Cuenot, T. Schmitt, S. Ducruix, S. Candel, Study of flame response to transverse acoustic modes from the LES of a 42-injector rocket engine, Proceedings of the Combustion Institute 36 (2017) 2633 – 2639. URL: `http://www.sciencedirect.com/science/article/pii/S1540748916301006`. doi:`https://doi.org/10.1016/j.proci.2016.06.042`.

[10] G. C. Cheng, R. Farmer, Real Fluid Modeling of Multiphase Flows in Liquid Rocket Engine Combustors, Journal of Propulsion and Power 22 (2006) 1373–1381. URL: `https://doi.org/10.2514/1.17272`. doi:`10.2514/1.17272`.

[11] M. Ishii, Thermo-fluid dynamics of two-phase flow, 2nd ed ed., Springer, New York, 2011.

[12] F. Baillot, J.-B. Blaisot, G. Boisdron, C. Dumouchel, Behaviour of an air-assisted jet submitted to a transverse high-frequency acoustic field, Journal of Fluid Mechanics 640 (2009) 305–342. doi:`10.1017/S002211200999139X`.

[13] J. S. Hardi, H. C. G. Martinez, M. Oschwald, B. B. Dally, LOx Jet Atomization Under Transverse Acoustic Oscillations, Journal of Propulsion and Power 30 (2014) 337–349. URL: `https://doi.org/10.2514/1.B34979`. doi:`10.2514/1.B34979`.

[14] T. Ménard, S. Tanguy, A. Berlemont, Coupling level set/VOF/ghost fluid methods: Validation and application to 3D simulation of the primary break-up of a liquid jet, International Journal of Multiphase Flow 33 (2007) 510–524. URL: `http://linkinghub.elsevier.com/retrieve/pii/S0301932206001832`. doi:`10.1016/j.ijmultiphaseflow.2006.11.001`.

[15] D. Fuster, A. Bague, T. Boeck, L. L. Moyne, A. Leboissetier, S. Popinet, P. Ray, R. Scardovelli, S. Zaleski, Simulation of primary atomization with an octree adaptive mesh refinement and VOF method, International Journal of Multiphase Flow 35 (2009) 550–565.

[16] A. Desjardins, H. Pitsch, Detailed numerical investigation of turbulent atomization of liquid jets, Atomization and Sprays 20 (2010) 311–336.

[17] M. Herrmann, A parallel Eulerian interface tracking/Lagrangian point particle multi-scale coupling procedure, Journal of Computational Physics 229 (2010) 745–759. URL: `http://linkinghub.elsevier.com/retrieve/pii/S0021999109005543`. doi:`10.1016/j.jcp.2009.10.009`.

[18] M. Herrmann, On simulating primary atomization using the refined level set grid method, Atomization and Sprays 21 (2011) 283–301.

[19] B. Duret, J. Reveillon, T. Menard, F. Demoulin, Improving primary atomization modeling through DNS of two-phase flows, International Journal of Multiphase Flow 55 (2013) 130–137. URL: `http://linkinghub.elsevier.com/retrieve/pii/S0301932213000773`. doi:`10.1016/j.ijmultiphaseflow.2013.05.004`.

[20] Z. Bouali, B. Duret, F.-X. Demoulin, A. Mura, DNS analysis of small-scale turbulence-scalar interactions in evaporating two-phase flows, International Journal of Multiphase Flow 85 (2016) 326–335. URL: `http://linkinghub.elsevier.com/retrieve/pii/S030193221530149X`. doi:`10.1016/j.ijmultiphaseflow.2016.06.020`.

[21] A. Vallet, A. Burluka, R. Borghi, Development of an Eulerian model for the atomization of a liquid jet, Atomization and Sprays 11 (2001) 619–642.

[22] M. Pourouchottamane, F. Dupoirieux, M. Habiballah, Cryogenic dense spray modelling using an interface density equation, in: 37th Joint Propulsion Conference and Exhibit, American Institute of Aeronautics and Astronautics, 2001. URL: `https://doi.org/10.2514/6.2001-3273`. doi:`10.2514/6.2001-3273`.

[23] F.-X. Demoulin, P.-A. Beau, G. Blokkeel, A. Mura, R. Borghi, A new model for turbulent flows with large density fluctuations: application to liquid atomization, Atomization and Sprays 17 (2007) 315–345. URL: `http://www.dl.begellhouse.com/journals/6a7c7e10642258cc,6fb83a3f452f6bb8,30fb5d541f3b4155.html`. doi:`10.1615/AtomizSpr.v17.i4.20`.

[24] J. Chesnel, J. Reveillon, T. Menard, F.-X. Demoulin, Large eddy simulation of liquid jet atomization, Atomization and Sprays 21 (2011) 711–736. URL: `http://www.dl.begellhouse.com/journals/6a7c7e10642258cc,3ca32fb40c63ad5e,29716d157a25e5e1.html`. doi:`10.1615/AtomizSpr.2012003740`.

[25] F.-X. Demoulin, J. Reveillon, B. Duret, Z. Bouali, P. Desjonqueres, T. Menard, Toward using direct numerical simulation to improve primary break-up modeling, Atomization and Sprays 23 (2013) 957–980. URL: `http://www.dl.begellhouse.com/journals/6a7c7e10642258cc,445ba8070f5787a9,1f0009ee4009367a.html`. doi:`10.1615/AtomizSpr.2013007439`.

[26] A. Refloch, B. Courbet, A. Murrone, P. Villedieu, C. Laurent, P. Gilbank, J. Troyes, L. Tessé, G. Chaineray, J. Dargaud, E. Quémerais, F. Vuillot, CEDRE Software, AerospaceLab Journal 2 (2011) 131–140.

[27] F. Laurent, A. Sibra, F. Doisneau, Two-Size Moment Multi-Fluid Model: A Robust and High-Fidelity Description of Polydisperse Moderately Dense Evaporating Sprays, Communications in Computational Physics 20 (2016) 902–943. URL: `http://www.journals.cambridge.org/abstract_S181524061600102X`. doi:`10.4208/cicp.300615.050216a`.

[28] A. Sibra, J. Dupays, A. Murrone, F. Laurent, M. Massot, Simulation of reactive polydisperse sprays strongly coupled to unsteady flows in solid rocket motors: Efficient strategy using Eulerian Multi-Fluid methods, Journal of Computational Physics 339 (2017) 210–246. URL: `http://linkinghub.elsevier.com/retrieve/pii/S0021999117300967`. doi:`10.1016/j.jcp.2017.02.003`.

[29] J. Chesnel, T. Menard, J. Reveillon, F.-X. Demoulin, Subgrid analysis of liquid jet atomization, Atomization and Sprays 21 (2011) 41–67. URL: `http://www.dl.begellhouse.com/journals/6a7c7e10642258cc,6fbc20a3389286f3,56977dbd27a3bf40.html`. doi:`10.1615/AtomizSpr.v21.i1.40`.

[30] J. Brackbill, D. Kothe, C. Zemach, A continuum method for modeling surface tension, Journal of Computational Physics 100 (1992) 335–354. URL: `http://linkinghub.elsevier.com/retrieve/pii/002199919290240Y`. doi:`10.1016/0021-9991(92)90240-Y`.

[31] E. Goncalvès, Modeling for non isothermal cavitation using 4-equation models, International Journal of Heat and Mass Transfer 76 (2014) 247 – 262. URL: `http://www.sciencedirect.com/science/article/pii/S0017931014003780`. doi:`https://doi.org/10.1016/j.ijheatmasstransfer.2014.04.065`.

[32] A. Chiapolino, P. Boivin, R. Saurel, A simple and fast phase transition relaxation solver for compressible multicomponent two-phase flows, Computers & Fluids 150 (2017) 31–45. URL: `http://linkinghub.elsevier.com/retrieve/pii/S0045793017301032`. doi:`10.1016/j.compfluid.2017.03.022`.

[33] N. Grenier, J.-P. Vila, P. Villedieu, An accurate low-Mach scheme for a compressible two-fluid model applied to free-surface flows, Journal of Computational Physics 252 (2013) 1–19. URL: `http://linkinghub.elsevier.com/retrieve/pii/S0021999113004312`. doi:`10.1016/j.jcp.2013.06.008`.

[34] P. Downar-Zapolski, Z. Bilicki, L. Bolle, J. Franco, The non-equilibrium relaxation model for one-dimensional flashing liquid flow, International Journal of Multiphase Flow 22 (1996) 473 – 483. URL: `http://www.sciencedirect.com/science/article/pii/030193229500078X`. doi:`https://doi.org/10.1016/0301-9322(95)00078-X`.

[35] D. A. Drew, Theory of multicomponent fluids, number 135 in Applied mathematical sciences, Springer, New York, 1999.

[36] M. R. Baer, J. W. Nunziato, A Two-phase Mixture Theory for the Deflagration-to-Detonation Transition (DDT) in Reactive Granular Materials, Journal of Multiphase flows 12 (1986) 861–889.

[37] R. Saurel, R. Abgrall, A Multiphase Godunov Method for Compressible Multifluid and Multiphase Flows, Journal of

Computational Physics 150 (1999) 425–467. URL: `http://linkinghub.elsevier.com/retrieve/pii/S0021999199961879`. doi:`10.1006/jcph.1999.6187`.

[38] P. Cordesse, M. Massot, Entropy supplementary conservation law for non-linear systems of PDEs with non-conservative terms: application to the modelling and analysis of complex fluid flows using computer algebra (2019).

[39] P. Cordesse, S. Kokh, R. D. Battista, F. Drui, M. Massot, Derivation of a two-phase flow model with two-scale kinematics, geometric variables and surface tension using variational calculus (2019).

[40] P. Cordesse, A. Remigi, B. Duret, A. Murrone, T. Ménard, F.-X. Demoulin, M. Massot, Validation strategy of reduced-order two-fluid flow models based on a hierarchy of direct numerical simulations (2019).

[41] F. A. Williams, Spray Combustion and Atomization, Physics of Fluids 1 (1958) 541. URL: `http://scitation.aip.org/content/aip/journal/pof1/1/6/10.1063/1.1724379`. doi:`10.1063/1.1724379`.

[42] O. Emre, D. Kah, S. Jay, Q.-H. Tran, A. Velghe, S. de Chaisemartin, R. O. Fox, F. Laurent, M. Massot, Eulerian moment methods for automotive sprays, Atomization and Sprays 25 (2015) 189–254. URL: `http://www.dl.begellhouse.com/journals/6a7c7e10642258cc,646ee0fc50ef4107,2146538f3762c926.html`. doi:`10.1615/AtomizSpr.2015011204`.

[43] Y. Tambour, A sectional model for evaporation and combustion of sprays of liquid fuels, Israel Journal of Technology 18 (1980).

[44] J. Greenberg, I. Silverman, Y. Tambour, On the origins of spray sectional conservation equations, Combustion and Flame 93 (1993) 90–96. URL: `http://linkinghub.elsevier.com/retrieve/pii/001021809390085H`. doi:`10.1016/0010-2180(93)90085-H`.

[45] F. Laurent, M. Massot, Multi-fluid modelling of laminar polydisperse spray flames: origin, assumptions and comparison of sectional and sampling methods, Combustion Theory and Modelling 5 (2001) 537–572. URL: `http://www.tandfonline.com/doi/abs/10.1088/1364-7830/5/4/303`. doi:`10.1088/1364-7830/5/4/303`.

[46] F. Doisneau, Eulerian modeling and simulation of polydisperse moderately dense coalescing spray flows with nanometric-to-inertial droplets: application to Solid Rocket Motors, Ph.D. thesis, Ecole Centrale Paris, 2013.

[47] W. A. Sirignano, The Formulation of Spray Combustion Models: Resolution Compared to Droplet Spacing, Journal of Heat Transfer 108 (1986) 633. URL: `http://HeatTransfer.asmedigitalcollection.asme.org/article.aspx?articleid=1439066`. doi:`10.1115/1.3246983`.

[48] W. A. Sirignano, Volume averaging for the analysis of turbulent spray flows, International Journal of Multiphase Flow 31 (2005) 675–705. URL: `http://linkinghub.elsevier.com/retrieve/pii/S0301932205000340`. doi:`10.1016/j.ijmultiphaseflow.2005.02.005`.

[49] G. Dufour, M. Massot, P. Villedieu, Étude d'un modèle de fragmentation secondaire pour les brouillards de gouttelettes, Comptes Rendus Mathematique 336 (2003) 447 – 452. URL: `http://www.sciencedirect.com/science/article/pii/S1631073X03000670`. doi:`https://doi.org/10.1016/S1631-073X(03)00067-0`.

[50] G. Dufour, Modélisation multi-fluide eulérienne pour les écoulements diphasiques à inclusions dispersees, Ph.D. thesis, Université Paul Sabatier Toulouse III, 2005.

[51] L. Vingert, M. Habiballah, Test case RCM-2 Mascotte single injector - 10 bar -, in: O. J. Haidn (Ed.), 2nd International Workshop on Rocket Combustion Modeling, Atomization, Combustion and Heat Transfer, Lampoldshausen, Germany, 2001.

[52] M. Habiballah, M. Orain, F. Grisch, L. Vingert, P. Gicquel, Experimental studies of high-pressure cryogenic flames on the MASCOTTE facility, Combustion Science and Technology 178 (2006) 101–128. URL: `https://doi.org/10.1080/00102200500294486`. doi:`10.1080/00102200500294486`.

[53] S. Candel, M. Juniper, G. Singla, P. Scouflaire, C. Rolon, Structure and dynamics of cryogenic flames at supercritical pressure, Combustion Science and Technology 178 (2006) 161–192. URL: `https://doi.org/10.1080/00102200500292530`. doi:`10.1080/00102200500292530`.

[54] P. Marmottant, E. Villermaux, On spray formation, Journal of Fluid Mechanics 498 (2004) 73–111. URL: `http://www.journals.cambridge.org/abstract_S0022112003006529`. doi:`10.1017/S0022112003006529`.

[55] S. B. Pope, Turbulent flows, Cambridge University Press, 2000.

[56] N. Ko, H. Au, Coaxial jets of different mean velocity ratios, Journal of Sound and Vibration 100 (1985) 211–232. URL: `https://linkinghub.elsevier.com/retrieve/pii/0022460X8590416X`. doi:`10.1016/0022-460X(85)90416-X`.

[57] E. Toro, M. Spruce, W. Speares, Restoration of the contact surface in the HLL-Riemann solver, Shock Waves 4 (1994) 25–34. URL: `http://dx.doi.org/10.1007/BF01414629`. doi:`10.1007/BF01414629`.

[58] C. Le Touze, A. Murrone, H. Guillard, Multislope MUSCL method for general unstructured meshes, Journal of Computational Physics 284 (2015) 389–418. URL: `http://linkinghub.elsevier.com/retrieve/pii/S0021999114008493`. doi:`10.1016/j.jcp.2014.12.032`.

[59] T. Buffard, S. Clain, Monoslope and multislope MUSCL methods for unstructured meshes, Journal of Computational Physics 229 (2010) 3745–3776. URL: `http://linkinghub.elsevier.com/retrieve/pii/S0021999110000495`. doi:`10.1016/j.jcp.2010.01.026`.

[60] B. van Leer, Towards the ultimate conservative difference scheme. V. A second-order sequel to Godunov's method, Journal of Computational Physics 32 (1979) 101–136. URL: `http://linkinghub.elsevier.com/retrieve/pii/0021999179901451`. doi:`10.1016/0021-9991(79)90145-1`.

[61] L. Schiller, Z. Naumann, A drag coefficient correlation, Ver. Deutsch. Ing. (1935) 77–318.

[62] B. Abramzon, W. Sirignano, Droplet vaporization model for spray combustion calculations, International Journal of Heat and Mass Transfer 32 (1989) 1605–1618. URL: `http://linkinghub.elsevier.com/retrieve/pii/0017931089900434`. doi:`10.1016/0017-9310(89)90043-4`.

[63] M. Pilch, C. Erdman, Use of breakup time data and velocity history data to predict the maximum size of stable fragments for acceleration-induced breakup of a liquid drop, International Journal of Multiphase Flow 13 (1987) 741–757. URL: `http://linkinghub.elsevier.com/retrieve/pii/0301932287900632`. doi:`10.1016/0301-9322(87)90063-2`.

[64] K. Wert, A rationally-based correlation of mean fragment size for drop secondary breakup, International Journal of Multiphase Flow 21 (1995) 1063–1071. URL: `http://linkinghub.elsevier.com/retrieve/pii/030193229500036W`. doi:`10.1016/0301-9322(95)00036-W`.

[65] D. Veynante, L. Vervisch, Turbulent combustion modeling, Progress in Energy and Combustion Science 28 (2002) 193–266. URL: `http://linkinghub.elsevier.com/retrieve/pii/S036012850100017X`. doi:`10.1016/S0360-1285(01)00017-X`.

[66] J. Abraham, F. Bracco, R. Reitz, Comparisons of computed and measured premixed charge engine combustion, Combustion and Flame 60 (1985) 309–322. URL: `http://linkinghub.elsevier.com/retrieve/pii/0010218085900367`. doi:`10.1016/0010-2180(85)90036-7`.

[67] Z. Ren, G. M. Goldin, An efficient time scale model with tabulation of chemical equilibrium, Combustion and Flame 158 (2011) 1977–1979. URL: `http://linkinghub.elsevier.com/retrieve/pii/S0010218011000721`. doi:`10.1016/j.combustflame.2011.02.018`.

[68] L.-H. Dorey, P. Grenard, L. Matuszewski, L. Selle, Experimental and Numerical Study of a Cooled Rocket Combustion Chamber, in: International Heat Transfer Conference 15, Begellhouse, 2014. URL: `http://www.ihtcdigitallibrary.com/conferences/ihtc15,08fa4b120d76fe39,3eb9f09845ca78e5.html`. doi:`10.1615/IHTC15.cmb.009238`.

[69] N. Fdida, L. Vingert, A. Ristori, Y. L. Sant, Droplet size and velocity measurements in a cryogenic jet flame of a rocket-type combustor using high-speed imaging, Atomization and Sprays 26 (2016) 411–438.

[70] N. Fdida, L. Vingert, G. Ordonneau, S. Petitot, Coupling high-speed imaging diagnostics to study a LOX/GH2 flame in a hig-pressure rocket combustor, in: 5th European Conference for Aeronautics and Space Sciences, Munich, Germany, 2013, pp. 1–13.

[71] E. Villermaux, Mixing and Spray Formation in Coaxial Jets, Journal of Propulsion and Power 14 (1998) 807–817. URL:

https://arc.aiaa.org/doi/10.2514/2.5344. doi:10.2514/2.5344.

[72] J. C. Lasheras, E. J. Hopfinger, Liquid Jet Instability and Atomization in a Coaxial Gas Stream, Annual Review of Fluid Mechanics 32 (2000) 275–308. URL: http://www.annualreviews.org/doi/10.1146/annurev.fluid.32.1.275. doi:10.1146/annurev.fluid.32.1.275.

[73] H. Eroglu, N. Chigier, Z. Farago, Coaxial atomizer liquid intact lengths, Physics of Fluids A: Fluid Dynamics 3 (1991) 303–308. URL: http://aip.scitation.org/doi/10.1063/1.858139. doi:10.1063/1.858139.

[74] R. Woodward, S. Pal, S. Farhangi, R. Santoro, LOX/GH2 Shear Coaxial Injector Atomization Studies at Large Momentum Flux Ratios, in: 42nd AIAA/ASME/SAE/ASEE Joint Propulsion Conference & Exhibit, American Institute of Aeronautics and Astronautics, Sacramento, California, 2006. URL: http://arc.aiaa.org/doi/abs/10.2514/6.2006-5203. doi:10.2514/6.2006-5203.

[75] F. Xiao, M. Dianat, J. McGuirk, LES of turbulent liquid jet primary breakup in turbulent coaxial air flow, International Journal of Multiphase Flow 60 (2014) 103–118. URL: https://linkinghub.elsevier.com/retrieve/pii/S0301932213001985. doi:10.1016/j.ijmultiphaseflow.2013.11.013.

[76] G. Charalampous, Y. Hardalupas, A. Taylor, Structure of the Continuous Liquid Jet Core during Coaxial Air-Blast Atomisation, International Journal of Spray and Combustion Dynamics 1 (2009) 389–415. URL: http://journals.sagepub.com/doi/10.1260/175682709789685840. doi:10.1260/175682709789685840.

[77] N. Rutard, L.-H. Dorey, C. Le Touze, S. Ducruix, Large-eddy simulation of an air-assisted liquid jet under a high-frequency transverse acoustic forcing, International Journal of Multiphase Flow 122 (2020) 103144. URL: https://linkinghub.elsevier.com/retrieve/pii/S0301932219300655. doi:10.1016/j.ijmultiphaseflow.2019.103144.

[78] F. Grisch, P. Bouchardy, W. Clauss, CARS thermometry in high pressure rocket combustors, Aerospace Science and Technology 7 (2003) 317–330. URL: http://linkinghub.elsevier.com/retrieve/pii/S1270963803000178. doi:10.1016/S1270-9638(03)00017-8.

[79] P. Gicquel, L. Vingert, Flow investigations of cryogenic sprays in combustion at sub and supercritical conditions, in: 16th Annual Conference on Liquid Atomization and Spray Systems, Darmstadt, Germany, 2000.

[80] N. Fdida, L. Vingert, Y. Mauriot, L.-H. Dorey, M. Théron, Comparison of LOX/Methane and LOX/Hydrogen cryogenic spray combustion with simultaneous optical diagnostics, in: EUCASS 2019, MADRID, Spain, 2019, pp. 1–10. URL: https://hal.archives-ouvertes.fr/hal-02320211.

[81] B. J. G. Mcbride, Coefficients for calculating thermodynamic and transport properties of individual species, Technical Report, 1993. URL: https://ntrs.nasa.gov/search.jsp?R=19940013151.

[82] W. Sutherland, The viscosity of gases and molecular force, Philosophical Magazine Series 5 36 (1893) 507–531. URL: http://www.tandfonline.com/doi/abs/10.1080/14786449308620508. doi:10.1080/14786449308620508.